Collapse Mechanisms of Small-Scale Unreinforced Masonry Vaults

by

Elaine Elizabeth Shapiro

B.S. Civil and Environmental Engineering
Virginia Polytechnic Institute and State University, 2010

Submitted to the Department of Architecture
in partial fulfillment of the requirements for the degree of

Master of Science in Building Technology

at the

Massachusetts Institute of Technology

June 2012

Author .....
Department of Architecture
May 11, 2012

Certified by .....
John A. Ochsendorf
Associate Professor of Building Technology and
Civil and Environmental Engineering
Thesis Supervisor

Accepted by .....
Takehiko Nagakura
Associate Professor of Design and Computation
Chair if the Department Committee on Graduate Students

Collapse Mechanisms of Small-Scale Unreinforced Masonry Vaults

by

Elaine Elizabeth Shapiro

Submitted to the Department of Architecture on May 11, 2012
in partial fulfillment of the requirements for the degree of
Master of Science in Building Technology

ABSTRACT

The structural behavior of masonry arches under various forms of loading is well-studied; however, the three-dimensional behavior of barrel vaults and groin vaults is not as well understood. This thesis aims to address this problem by performing scale model testing of barrel and groin vaults as a complement to analytical solutions. The behavior of the model vaults are observed in four cases: (1) spreading supports, (2) vertical point loads applied at various locations of the vault's geometry, (3) point loads applied to an initially deformed vault, and (4) horizontal acceleration through tilting.

In all cases, extensive experimental testing is carried out on a subset of three model vaults: two barrels and one groin vault, all with the same radius and thickness ratio but with different angles of embrace. High-speed cameras are used to capture the collapse mechanism of the vaults. The analyses include equilibrium methods executed through Excel and Matlab programs, publicly available online applets for arch stability, and hand calculations.

The testing and analysis carried out in this thesis reveal several properties that can be used by engineers studying existing structures. First, a groin vault's spreading capacity is determined by the constituent barrel vault that is spreading. This simplifies the analysis to a two-dimensional problem. Second, the load capacity of a barrel vault is linearly proportional to the initial deformation in span. So, if a vault experiences a span increase that is 25% of the maximum it can withstand, its load capacity decreases by 25%. Nearly all vaults have experienced deformations due to settlement over time and will therefore respond differently to loading than a perfect vault which is the common starting point in analysis. This work can be applied to the understanding and maintenance of masonry vaults in service throughout the world.

Thesis Supervisor: John A. Ochsendorf
Title: Associate Professor of Building Technology and
Civil and Environmental Engineering

Acknowledgements

First, I would like to thank my advisor, John Ochsendorf, for his support and excitement for historic masonry, which inspired me to tackle these questions.

Next, I acknowledge financial support for this work provided by a National Science Foundation Graduate Research Fellowship and TODA funds through the Building Technology Program at MIT.

Additionally, I am grateful to many individuals who helped along the way to make the experimental testing possible. I could not have completed the many hours of model fabrication and testing without the help of Kenya Mejia who was supported by the MIT Undergraduate Research Opportunities Program. Aissata Nutzel and Alvaro Quinonez created the initial model blocks. Ken Stone and Brian Chan of the MIT Hobby Shop gave essential instruction and design help for constructing the formwork and platforms that made the vault building possible. Jim Bales of the Edgerton Center shared the high-speed cameras along with detailed instructions for their use. Steve Rudolph of the Civil Engineering Department coordinated use of the lab space and data acquisition design for the experiments.

Jennifer Zessin was an incredible resource throughout the last two years and graciously shared her Matlab functions for me to adapt to my own uses. Also, I would like to thank the faculty and staff of BT for their assistance throughout the program.

Finally, I would like to thank my parents, family, and friends, both in the BT lab and farther away, for their support, advice, and kind words. And, most of all, I thank Brad for his enduring encouragement and enthusiasm.

Contents

Chapter 1

Introduction

Masonry construction dominates the landscape of structures built before the end of the nineteenth century (Heyman 1995). While it is rare for new unreinforced masonry structures to be built today, many historical masonry buildings are still in use. In some cases, these buildings have survived hundreds of years of settlement and deterioration. It is necessary for contemporary engineers to be able to accurately assess masonry structures in order to appropriately maintain them as historic landmarks and eliminate potentially hazardous situations.

Current engineering education and practice focuses on steel and reinforced concrete structures, which are primarily based on material strength and elasticity. However, safety in traditional masonry construction is often a problem of stability and geometry (Block et al. 2006). Modern materials allow for towering buildings and long span bridges to be built that would never be possible using unreinforced masonry. Unfortunately, this focus in current engineering education and practice has led to a break in understanding over the last few generations of how to analyze the collapse conditions for traditional masonry structures.

Over the years, a strong understanding of the load capacity of masonry arches has been created (Heyman 1982; Livesley 1992). However, the three-dimensional behavior of vaults is less well known (Boothby 2001). Complex methods have been developed to analyze masonry structures including computer simulations and numerical methods. These developments have been applied to a wide range of structures, including arches, domes, and flying buttresses, but the forms of barrel vaults and groin vaults have been neglected to a certain extent.

1.1 Problem Statement

This thesis explores the collapse mechanisms of barrel vaults and groin vaults experimentally and analytically. Physical and computational models are used to determine collapse limits due to:

1. Applied point loads
2. Spreading of the supports
3. Applied point loads on an initially deformed structure
4. Constant horizontal acceleration (through tilting)

The results of the physical models are supported by analytical approximations. The analysis is developed by expanding upon existing tools and methods. The aim of this thesis is to quantify failure modes and provide engineers with recommendations and tools for accurately assessing the current safety of barrel vaults and groin vaults in existing infrastructure.

1.2 Literature Review

A good number of methods and tools have been developed to understand arch behavior. It is useful to understand these methods so that they can be expanded to three dimensions to better explain the collapse mechanisms of vaults. More complex methods have been developed to analyze masonry structures including computer simulations and numerical methods.

1.2.1 Arch analysis

Traditional masonry arches, as mentioned previously, are stable primarily because of their geometry, not because of their material properties. The collapse mode of an arch can be determined based on the shape and self-weight of the arch plus the position at which the load is applied (Pippard et al. 1936). The capacity of these arches can be determined using an equilibrium calculation, commonly shown as a line of thrust. The thrust line represents the resultants of the stresses exerted at the interfaces between voussoirs (Heyman 1982). The compression forces at the interface must be in equilibrium with the self-weight and any external forces. The locus of pressure points is then represented as a thrust line (Figure 1.1).

The set of compressive forces can be found using graphical methods and equilibrium equations. Graphical methods involve creating a force polygon such as the one shown in Figure 1.2. A linear scale is established to represent force, then the vertical force acting on each voussoir, including self-weight and external loads, is drawn in the appropriate scale end-to-end as the base of the force polygon. Then, an initial value of horizontal thrust is established. This determines the angle of each segment of the polygon, which become the angle of the thrust line for the matching block of the arch. The horizontal thrust value can

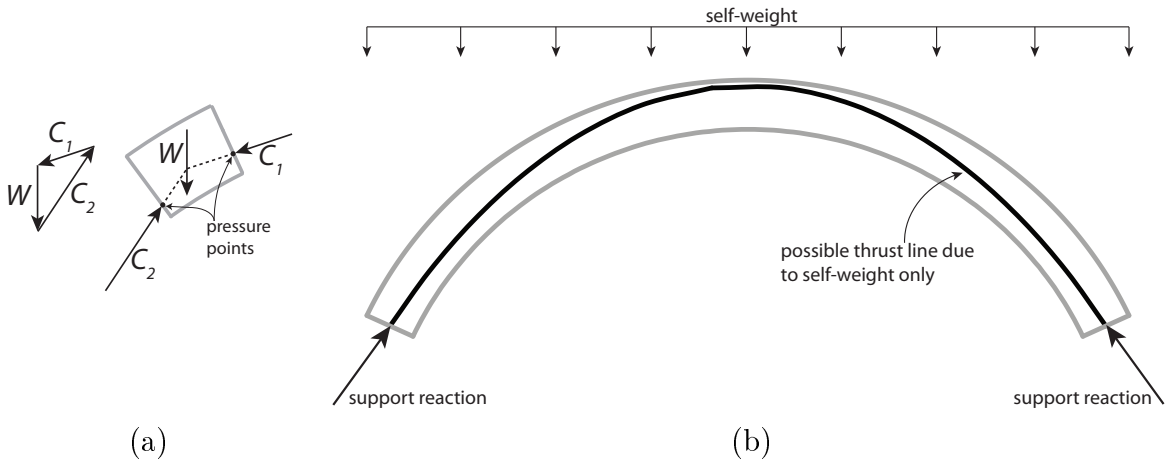

Figure 1.1: (a) Thrust line analysis assumes that all forces on each block of an arch are in equilibrium. (b) The thrust line is a visualization of the compressive forces within the arch. A possible thrust line for an arch due to self-weight only is shown.

be varied until the entire line lies within the masonry. This method is entirely graphical and does not require calculation, making it an efficient tool for designers of vaulted masonry (Allen and Zalewski 2010). Figure 1.2 is a special case because it shows the minimum thickness ratio for an arch of 180°. This is evidenced by the thrust line lying just within the masonry.

The location of the thrust line can also be determined using equilibrium equations. Global equilibrium is used to solve for the horizontal and vertical reactions at the abutments. Then, the location of the thrust line at each block interface can be solved using local equilibrium.

A rigid arch is indeterminate to the third degree (Ochsendorf and Romano 2010), meaning that an infinite set of possible thrust lines can be found that represent the forces within a typical arch. The lines can be defined given the horizontal force and the location of the line at two points within the arch. A lower bound solution, is any one of these thrust lines that meet the requirements of stability. If the supports move, hinges typically form to accommodate this displacement. The hinges reveal points where the thrust line must act because only a single point of contact remains for the force to be transferred (Heyman 1995). The uniqueness theorem states that at collapse, one line of thrust can be found within the masonry. This collapse condition is also known as an upper bound solution.

Three main assumptions are made when analyzing historical masonry structures using classical limit analysis (Heyman 1982). First, masonry cannot carry tensile forces. This is a conservative assumption and is true for the most part. While individual blocks could carry some amount of tension before failing in a brittle manner, the mortar between the blocks carries a minimal amount and will separate. Second, friction between the voussoirs is

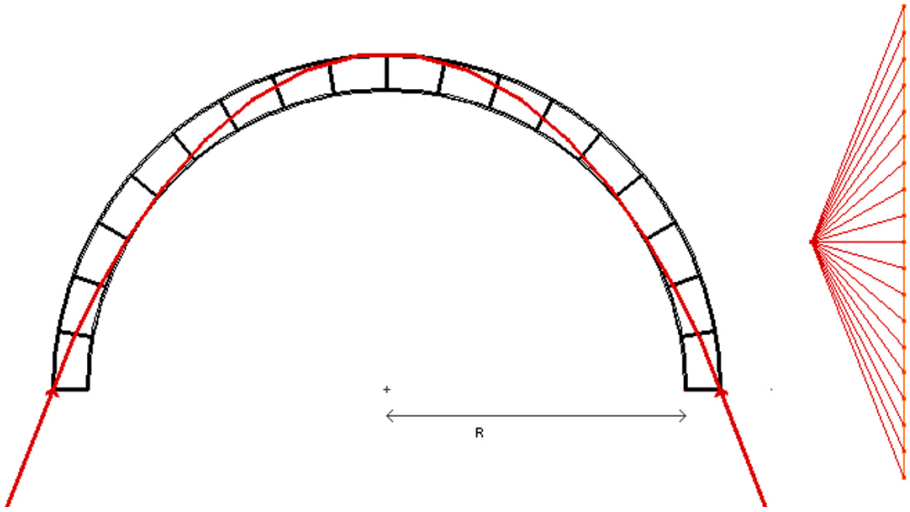

Figure 1.2: Graphical method of thrust line calculation. The force polygon to the right determines the angle of the thrust line for each block. The horizontal thrust is equal to the horizontal dimension of the triangle. (MIT Masonry 2012) This arch is the minimum thickness ratio for a 180° arch to stand only loaded by self-weight.

sufficient to prevent failure due to sliding of one voussoir relative to another. This assumption has been shown to be correct in practice, though in rare cases sliding can occur. Third, masonry has infinite compressive strength. This is an unsafe assumption. However, arches commonly fail as a result of mechanisms that are triggered at stresses, which are an order of magnitude lower than the crushing strength of stone. Also, while local crushing may occur at hinges, this typically does not affect the integrity of the system as a whole.

1.2.2 Collapse of arches due to spreading supports

A documented issue in historic buildings is the movement of buttress walls over time. Buttress walls can lean outwards due to differential settlement of foundations (Ochsendorf 2002). One example is the basilica at Vézelay, France, which has suffered extreme deformations over time, but still stands (Figure 1.3).

As the buttresses lean, the supports of the vault move, increasing the span, which causes the crown to lower and hinges to open in order to accommodate the shifting thrust line. The horizontal thrust increases as the supports spread until collapse. Ochsendorf (2006) has shown that span increase of an arch is dependent upon its thickness ratio, angle of embrace, and voussoir size. Tools to analyze the spreading failures of arches have been developed by Block et al. (2006).

The work discussed thus far has only assessed arch behavior and not delved into the three-dimensional world of barrel and groin vaults. While it may seem a logical step that barrel vaults follow the hinging pattern of arches, this has not been experimentally verified,

Figure 1.3: Many of the arches along the nave of Vézelay Abbey have suffered extreme deformations over time. As the span increases, the crown of an arch lowers and hinges open. The arches in the foreground have flattened, but those in the background remain circular. Photo credit: Isabel Tarrío

nor has the behavior of more complex groin vaults.

1.2.3 3D "Network analysis" of barrel vaults

The behavior of arches under various loading conditions including spreading supports has been studied extensively. However, the three dimensional action displayed by barrel vaults is discussed in only a limited number of papers. O'Dwyer (1999) proposes a force network model to analyze vaults. This method extends the idea of a line of thrust in an arch into a surface of thrust within a vault. This surface describes the resultants of forces within a vault.

The network is defined by a set of nodes and members. The nodes represent points where discrete forces are applied. These forces can include the self-weight and other distributed forces which have been discretized. The members represent possible paths the force can take between nodes. The results of the analysis are very dependent on these paths, so they must be chosen with the actual behavior of the vault in mind. The horizontal x- and y-coordinates are defined for each node. The height of the node, the z-coordinate, is undefined, but an envelope within which it can move is set by the geometry of the actual vault. The surface

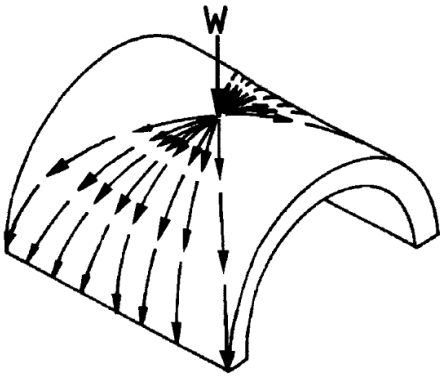

Figure 1.4: Possible force paths within a barrel vault (O'Dwyer, 1999)

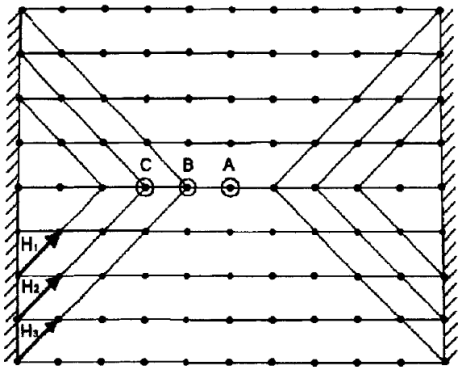

Figure 1.5: Nodal diagram of thrust network (O'Dwyer, 1999)

of thrust cannot pass outside of the geometry of the vault because that would represent tension occurring within the vault, which is impossible, just like the line of thrust cannot pass outside of the arch.

O'Dwyer illustrates the method with an example of a barrel vault. He argues that a point load applied to a barrel vault can take one of many paths to the abutment, and several of these options are shown in Figure 1.4. He then models the force network as in Figure 1.5 asserting that this network represents the most basic improvement to analyzing the load on a vault as being supported by a single arch rib. To investigate his argument, loads are applied at points A, B, and C in Figure 1.5 and the maximum capacity of the arch and vault of the same geometry are compared. It is found that the network model predicts a 325% increase in capacity over the arch when both are loaded at point A. The increase is only 116% for a load at point C, but it is clear that the vault benefits from providing many paths for the force to travel over to the abutments no matter where the load is applied.

More recently, Block and Ochsendorf (2007) have expanded upon these funicular methods by using the concept of duality between the geometry of a structure and the in-plane forces on each node. Graphic statics is also rooted in this theory. Block and Lachauer (2012) have

continued this work to analyze quadripartite vaults and applied the method to the intricate nave vaults of Sherborne Abbey in England. Both of these studies provide rigorous mathematical studies of possible thrust network conditions within vaults, however, they do not verify the predictions with physical testing. By providing experimental data, this thesis aims to round out the study of three-dimensionality in vaults.

1.2.4 Arch behavior under seismic conditions

Many masonry structures are located in seismic regions and have a varied history of success surviving large seismic events (DeJong 2009). The actual performance of these structures in earthquakes is very complex and difficult to predict. Investigations of arch behavior under impulse base motion (De Lorenzis et al. 2007) and rocking based on earthquake time histories (DeJong et al. 2008) have been done to begin to understand the two-dimensional behavior of arches due to these stresses. Just as with other failure loads, the arch will collapse when a four hinge mechanism forms. Clemente (1998) presents a model for stone arch behavior under base motion using a two part method. First, a static analysis is conducted to find the collapse mechanism, then the non-linear equation of motion is solved. Because of the complex nature of failure of vaults under earthquake loads, experimental data, including both collapse loads and footage of collapse, for barrel and groin vaults can expand the understanding of three-dimensional behavior.

1.2.5 Scale model contributions to masonry analysis

A novel approach for testing vaulted structures is creating physical scale models. Three-dimensional printing provides a unique opportunity to create detailed representations of vaulted structures at a cost much lower than full-size experiments. Additionally, calculations require significant assumptions about material properties and other modeling parameters (Quinonez et al. 2010). The addition of data from empirical models can enhance the value of numerical analysis. Because of the geometrical nature of masonry collapse analysis, structures can be scaled down for physical testing. This is true because material properties do not typically govern in collapse analysis of historical masonry. Scale models were used in medieval times by designers because the notion of scaling up geometry of masonry structures was well understood. Scale model experiments on domes have been performed by Zessin et al. (2010) to study the effect of supports spreading uniformly outwards. The results are compared to the cracking patterns of the Pantheon. Additionally, Van Mele et al. (2012) have done scale model testing of a model groin vault with differential settlement of one support.

1.3 Summary

This chapter has identified four areas of research in the performance of historic masonry barrel and groin vaults and discussed the previous work in each topic. There are several analysis methods that have been developed, most of which focus on arch behavior. However, this thesis will expand the work to include physical experiments, compare them to results from current techniques, and suggest new techniques for analyzing masonry vaults. Next, the experimental and analytical methodology will be discussed.

Chapter 2

Methodology

Three physical models are used for the experimental portion of this thesis: two barrel vaults and one groin vault. Each vault is made of individual blocks and is accompanied by a platform to serve as the abutments and formwork to facilitate the construction of the vault for repeated experiments. This chapter details the creation of the models as well as experimental set up and introduces the analysis methods.

2.1 Models

2.1.1 Model geometries

The geometrical properties of each model are summarized in Figure 2.1. All models have the same thickness ratio (0.138), radius, and voussoir size so that comparisons can be drawn between them.

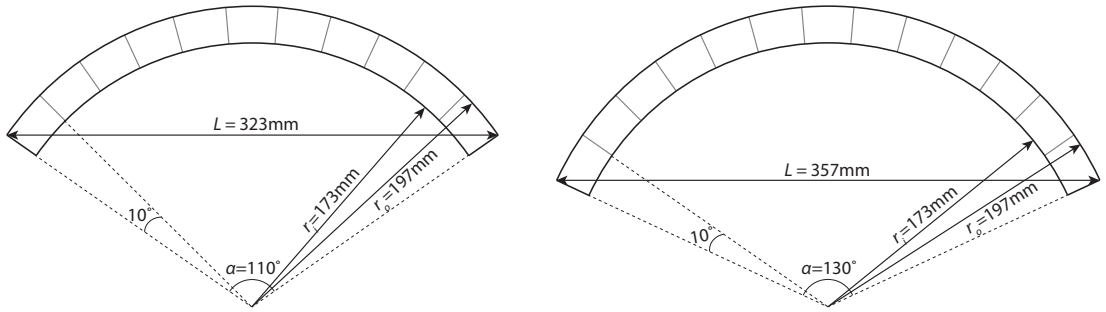

(a) (b)

Figure 2.1: Vault dimensions. (a) The first barrel vault (254 mm deep) and the constituent barrels of the groin vault (318 mm deep) have an angle of embrace of 110°. (b) The second barrel vault is 130° (254 mm deep). The thickness ratio of all vaults is 0.138.

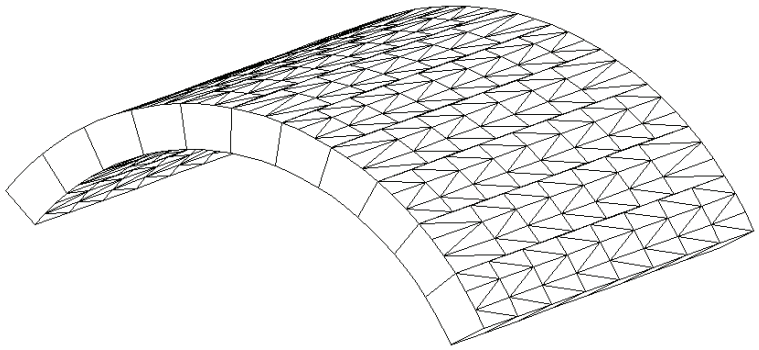

Figure 2.2: Computer model of 110° barrel vault showing interlocking rows of blocks.

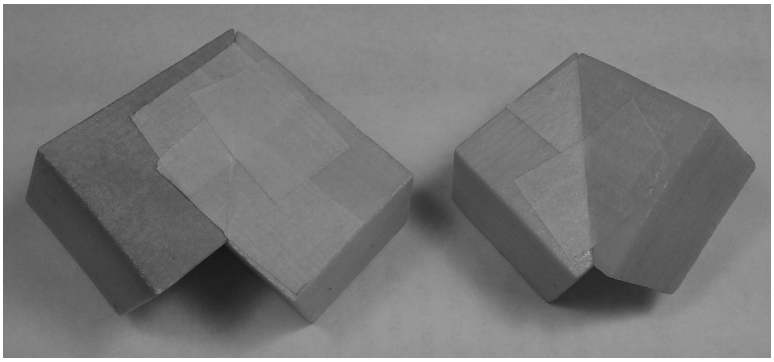

Figure 2.3: Two of the five block geometries used to form the groins

Figure 2.2 displays the computer model of the 110° barrel vault. Rows of blocks are either made up of eight blocks that are 32 mm deep or two blocks that are 48 mm deep and five blocks that are 32 mm deep. This creates the interlocking pattern between rows.

In addition to square blocks, the groin vault also requires special blocks to create the groins. There are five different geometries; two are shown in Figure 2.3. The blocks are fabricated as two mirror image components that are secured together with tape to realistically represent the construction of groin vaults. The performance of the groin vault is compared with the blocks along the groin both separate and fixed to its pair.

2.1.2 Model fabrication

First, the geometry of the vault is established in Rhinoceros (www.rhino3d.com) a modeling program. Then, it is transformed into an input file for the Z-Corp (www.zcorp.com) printer by separating and arranging the blocks in an appropriate space for the printer bed. The printer functions by laying adhesive on a bed of powder material then applying a thin layer of powder over the entire bed and repeating the process, changing the adhesive pattern with each layer to create the blocks. The blocks are allowed to dry in the bed and then

carefully excavated. Upon removal, the blocks are chalky and fragile so they are coated twice in polyurethane to increase the durability of the material and, therefore, preserve the initial shape.

Other key pieces of the models are the platform that serves as the abutments and the formwork that assists in the assembly of the vaults for repeated tests. The platform is designed so that one abutment (two adjacent supports for the groin vault) can move slowly away from the other when threaded rod is turned. This feature is used for the spreading support experiments and to create the initial displacements for the point load experiments on a deformed vault. The formwork is shaped to match the outer shell of the vaults so that the blocks can be laid in it upside down, then the platform placed on top and the entire assembly flipped over. This allows the vaults to be built efficiently for repeated testing.

2.2 Experimental Set-up and Procedure

All tests are recorded using high-speed video. This allows for the exact collapse mechanism to be observed. The specifics of each experiment are listed below.

2.2.1 Spreading supports

As mentioned previously, the abutments are designed to move apart as a threaded rod is turned. For each experiment, the model is erected in an undeformed state and the abutment is moved at a constant rate until the vault collapses. The maximum deformation is recorded.

2.2.2 Vertical point loads

Point loads are applied using a vertical arm that is slowly lowered using a hand crank (Figure 2.4). A cube with a divot is attached to the end of the arm so that the load can be applied through a sphere that sits between the arm and the vault. As the crank is turned and the arm lowers, the displacement and load are recorded, generating a load versus displacement plot in real time. The load is increased until the vault collapses.

These experiments are carried out on the barrel vault with an angle of embrace of 130° and the groin vault. The point loads are applied along a line at the center of the depth of the arch as shown in Figure 2.5.

2.2.3 Point loads on an initially deformed vault

For this experiment, the barrel vault with an angle of embrace of 130° is constructed as normal, then spread to 25, 50, and 75% of the maximum deformation established by the first experiment. Then, the procedures for the second experiment are followed.

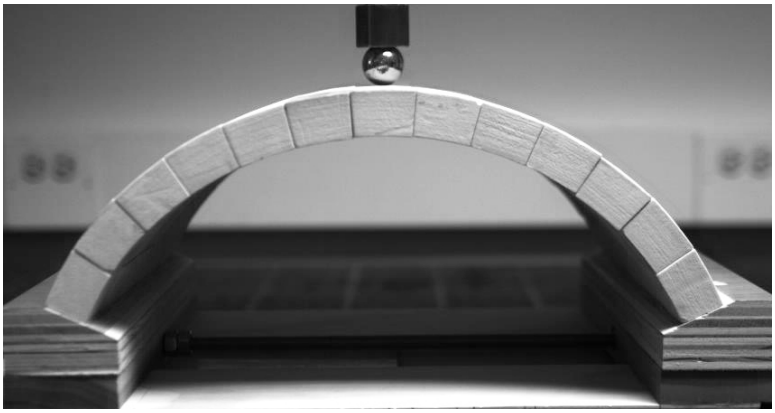

Figure 2.4: Point load application assembly. A vertical arm with a sphere at the end is lowered to simulate a true point load, while the displacement and load are measured.

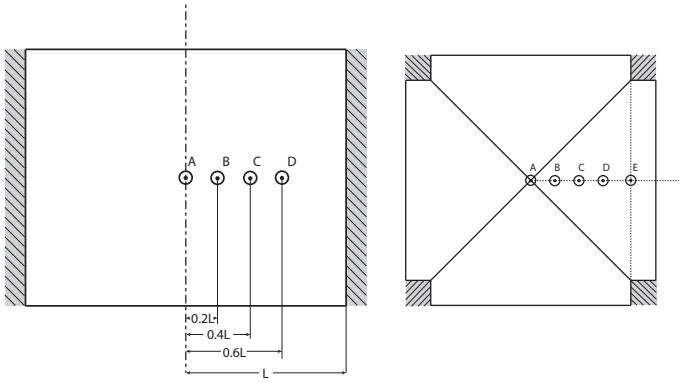

Figure 2.5: The barrel vault is loaded at midspan and 20, 40, and 60% of the half span. The groin vault is loaded in the same locations along an arm as well as near the edge.

2.2.4 Constant horizontal acceleration (through tilting)

The model is placed on a large tilting platform. As one end of the platform is raised, an inclinometer records the maximum angle of incline before collapse. The barrel vault with an angle of embrace of 130° and the groin vault are tested in this manner. The barrel vault is tilted in three orientations: with the abutments parallel, perpendicular, and 45° to the axis of rotation. Given the symmetry of the groin vault, it is only tested in the last two orientations (Figure 2.6).

2.3 Analytical Methods

Each experiment is accompanied by an appropriate mathematical analysis. These analyses include equilibrium methods executed through Excel and Matlab functions, publicly available online applets for arch capacity, and centroid analysis. The details of each will be discussed in the appropriate chapter.

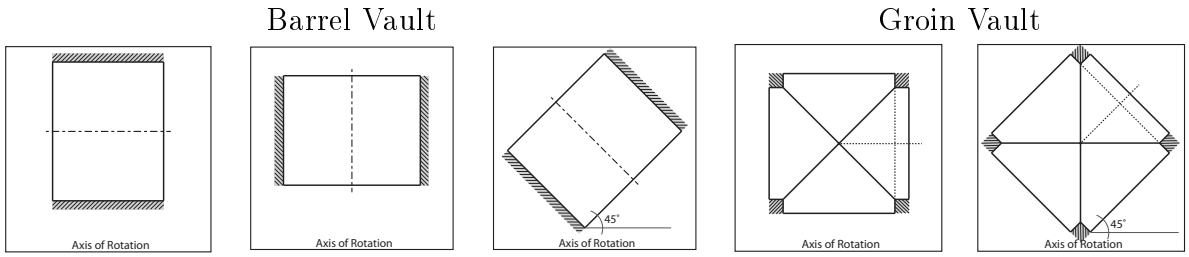

Figure 2.6: For the tilting experiments, the barrel vault is oriented parallel, perpendicular, and 45° to the axis of rotation. Due to the symmetry of the groin vault, it is only tilted in the last two orientations.

2.4 Summary

The experiments and analysis presented in this thesis are divided into four sections. Each includes repeated testing of scale models as well as analysis that can be used to predict behavior of existing structures. The spreading and point load results are used as a basis for the load capacity of deformed vaults. The first set of analysis discussed is the capacity of vaults to maintain stability with spreading supports.

Chapter 3

Vault capacity for spreading supports

It is common for the walls of masonry buildings to lean outwards over time as foundations settle. The span of vaults that are supported by these walls must increase to accommodate the movement. As the span increases, the horizontal thrust grows and puts additional pressure on the walls, causing them to spread farther, and the cycle continues. This chapter looks at the capacity of barrel and groin vaults to increase in span as their abutments move outwards over time.

3.1 Experimental Results

Scale model testing is done on the 130° barrel vault, 110° barrel vault, and groin vault. It is observed that the barrel vaults hinge along the lines of voussoirs, just as an arch made of very deep continuous blocks would. The hinging patterns are recorded using high-speed cameras. As one abutment begins to move away from the other, three hinges open (Figure 3.1.a). When two hinges open on the same side, it indicates that the thrust line is passing by the very edge of the vault at that location. This occurs when the hinge location is shifting (Figure 3.1.b). The vault collapses when the fourth hinge opens at the abutment (Figure 3.1.c) allowing all the segments to rotate and collapse.

The groin vault exhibits similar cracking patterns with an extrados hinge opening at the crown. The arms of the vault perpendicular to the direction of spreading begin to tilt along the crack and show a linear crack at the edge of the crossing barrel (Figure 3.2). The experiment is performed with the blocks along the groin separate as well as with the pairs fixed to each other. The spreading capacity is the same for both configurations.

The initial span and average results of all trials are summarized in Table 3.1. For results from all trials, see Appendix B.1.

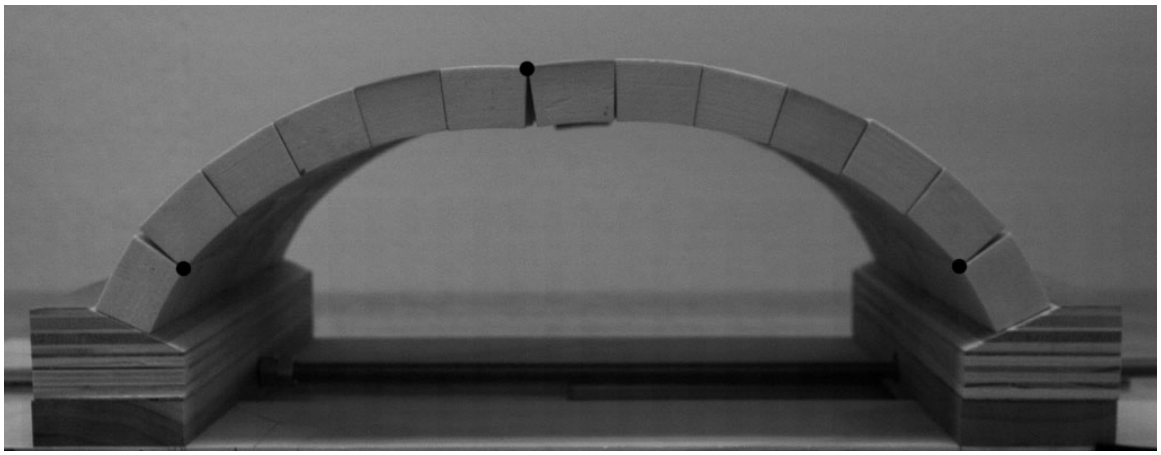

(a)

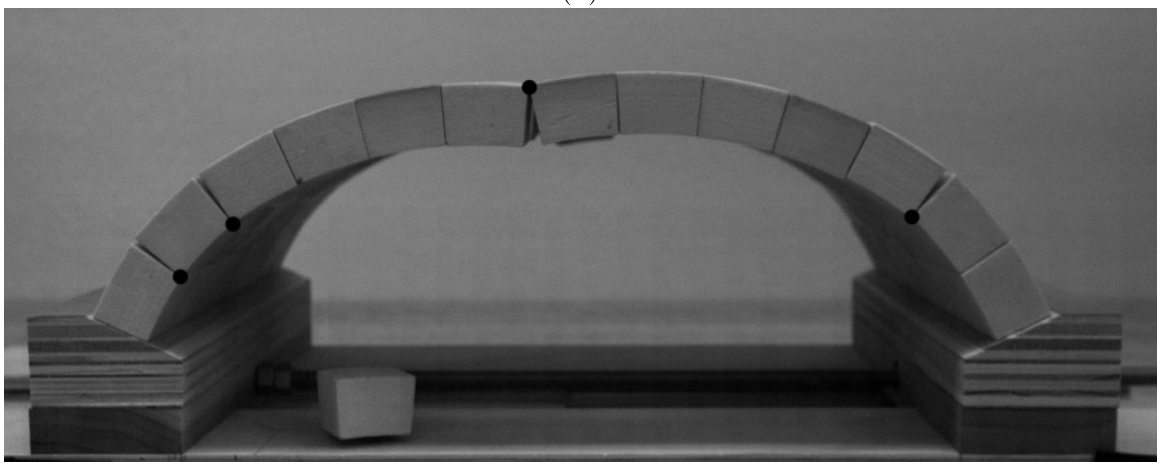

(b)

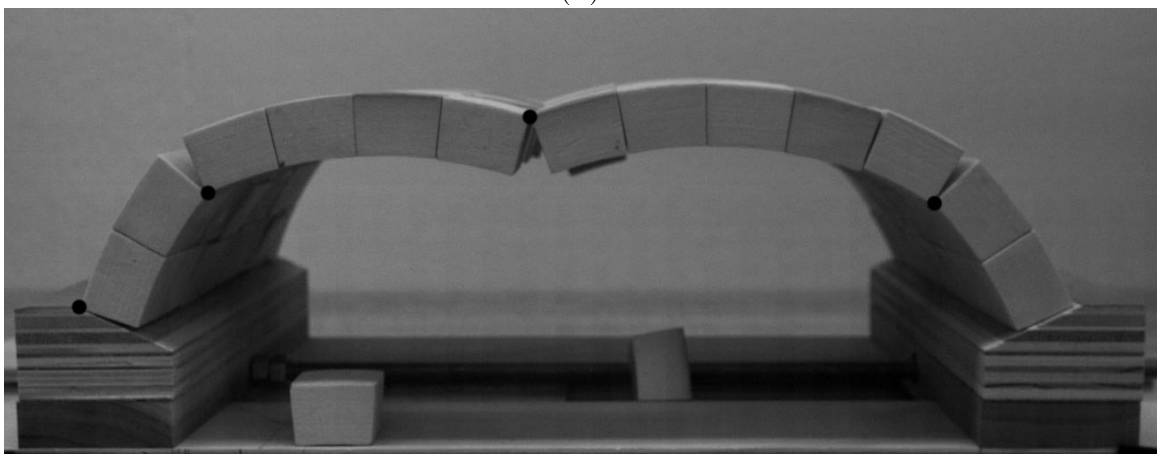

(c)

Figure 3.1: Hinging patterns of the 130° barrel vault (a) at partial deformation, (b) when hinge location is shifting, and (c) at collapse. Hinges are marked with black dots.

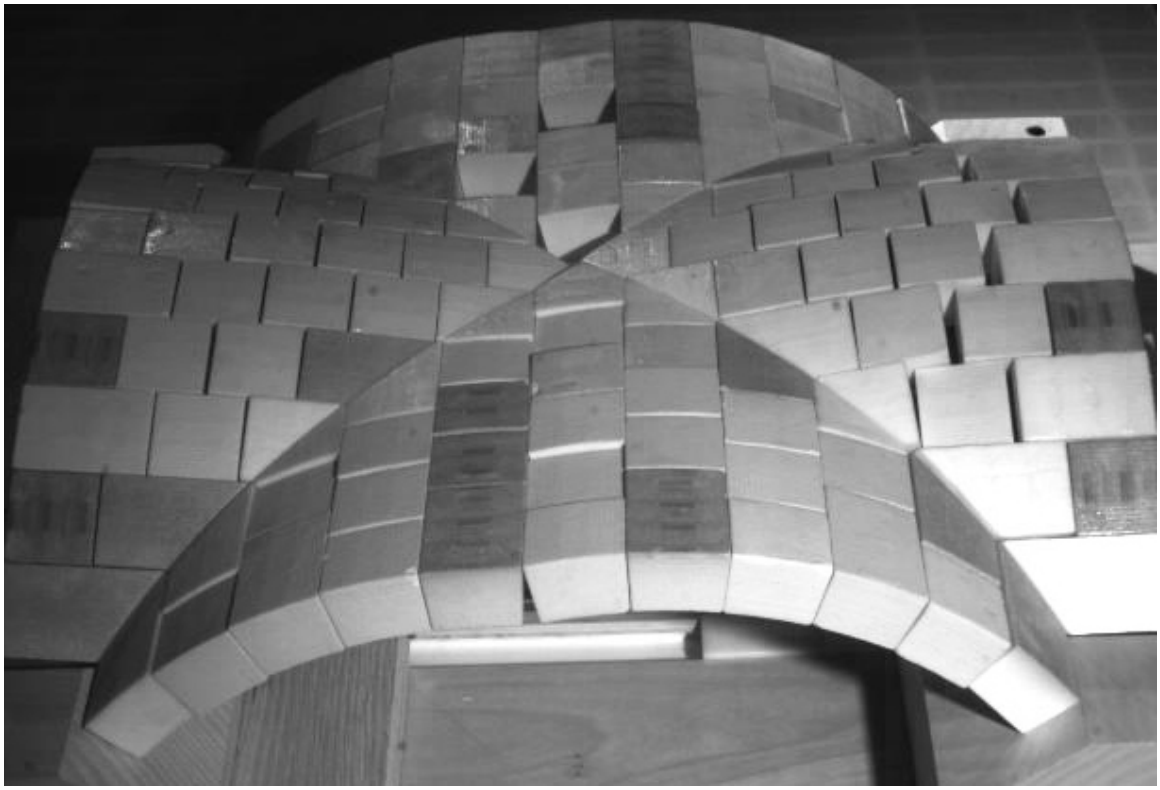

Figure 3.2: The groin vault cracks along the crown of the vault and the perpendicular arms crack linearly. A few blocks fall out at the crown, indicating that they do not carry any compression forces.

Table 3.1: Average vault span increase to cause collapse

	Initial Span [mm]	Distance Spread [mm]	Percent Increase
Barrel (130°)	308	23	7.5%
Barrel (110°)	278	26	9.4%
Groin (110°)	278	27	9.7%

3.2 Analytical Results

Two methods are used to predict the capacity of each vault to increase in span until collapse. The first is a publicly available applet called "Arch Collapse I," which is part of the InteractiveThrust suite available through the Masonry at MIT group website (web.mit.edu/masonry). The second is a Matlab code called BarrelSpread based on the DomeSpread code presented in Zessin's PhD dissertation (2012).

Due to repeated testing, the corners of the blocks suffered slight chipping, effectively rounding the corners and moving the actual hinge location towards the interior of the arch. To account for this in the calculations, an effective thickness of 80% of the perfect geometry

is compared to the capacity of the full thickness. This ratio is proven to accurately represent the behavior of arches by DeJong (2009).

3.2.1 InteractiveThrust

The "Arch Collapse I" applet of the InteractiveThrust suite (MIT Masonry 2012) allows the user to input the geometry of the arch, angle of embrace, and hinge locations by manipulating particular points on an image of an arch. As the user slides the abutment, increasing the span, the hinging geometry and thrust line update in real time. It is the responsibility of the user to identify the proper position for the maximum spread of the arch by moving the hinges and determining where the thrust line passes out of the arch. The applet assumes that the arch can hinge at the crown. This is not possible in the scale models used in this experiment as there is an odd number of blocks with one centered at the crown.

To simulate the scale models, the appropriate geometry is input into the applet and the hinge location is adjusted based on the voussoir size (Figures 3.3 and 3.4).

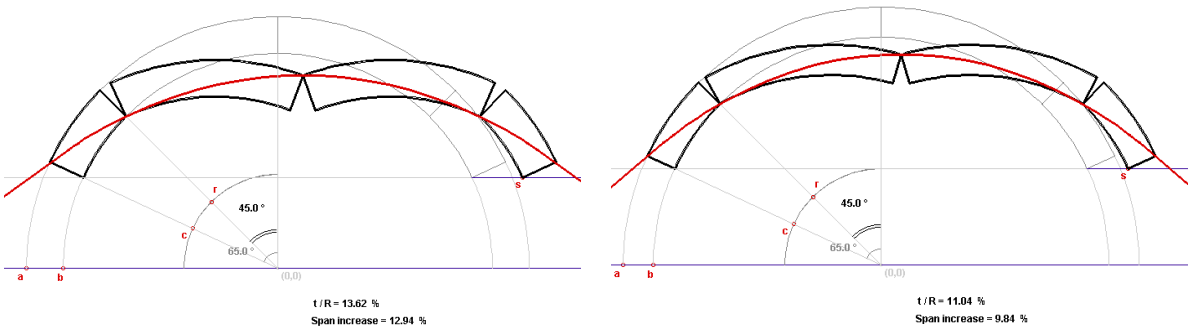

(a) (b)

Figure 3.3: InteractiveThrust results for a 130° arch of (a) full thickness and (b) effective thickness of 80%. The predicted increases are 12.9% and 9.8%, respectively.

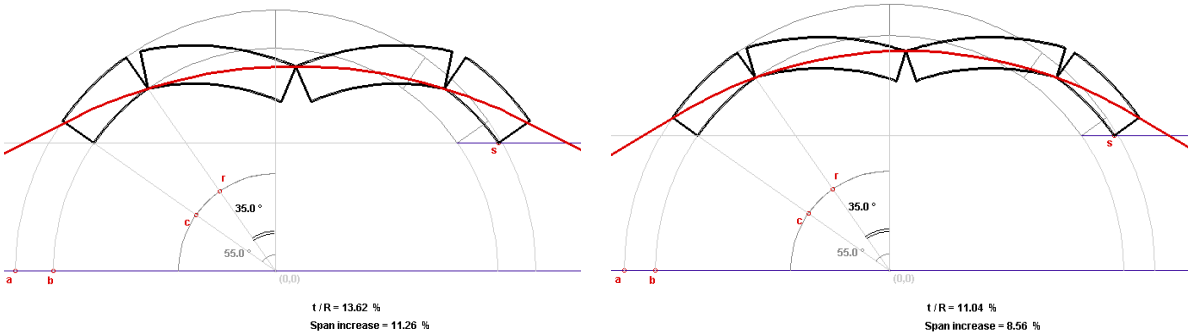

(a) (b)

Figure 3.4: InteractiveThrust results for a 110° arch of (a) full thickness and (b) effective thickness of 80%. The predicted increases are 11.3% and 8.6%, respectively.

3.2.2 Matlab simulations

The Matlab program, BarrelSpread, requires the user to input the angle of embrace, thickness ratio, and number of blocks in the arch. It calculates voussoir size and allows for a block to be centered at the crown of the arch. The program is a modified version of DomeSpread created by Zessin (2012) and the full code can be found in Appendix C.1.

BarrelSpread models half of an arch, assuming a symmetric hinging pattern. It operates by identifying three hinge locations - B, C, and D (Figure 3.5). B and C are fixed at the extrados and intrados, respectively, and D moves along the abutment as the thrust line is continually calculated. Each iteration begins with a small increment of displacement (dx) of segment CD to the right. Next, the vertical displacement (dy) is calculated using the geometry of the rotated segment BC (Eq. 3.1). Then, the horizontal thrust is calculated using the local equilibrium of segment BC (Eq. 3.2). The horizontal thrust is constant throughout the entire arch, so once that is determined, a local equilibrium equation can be solved to determine the position of D along the abutment in terms of a radius (r_d) from the center of segment CD (Eq. 3.3). When D reaches the extrados, the arch has attained its maximum spread, which is equal to dx/L (Figure 3.5). The predicted maximum span increases for an arches of 130° and 110° are shown in Figures 3.6 and 3.7, respectively.

$$dy = y_B - y_C - \sqrt{2\,(dx)\,x_B - 2\,(dx)\,x_C + {y_B}^2 + {y_C}^2 - dx^2 - 2y_B y_C} \tag{3.1}$$

$$\sum M_B = 0 = W_{AC}\,(x_C - x_B) - W_{BC}\,(\bar{x}_{BC} - x_B) - H\,(y_B - y_C) \tag{3.2}$$

$$\sum M_C = 0 = -W_{CD}\,(\bar{x}_{CD} - x_C) + W_{total}\,(r_d sin\alpha + dx + x_C) - H\,(y_C - r_d cos\alpha) \tag{3.3}$$

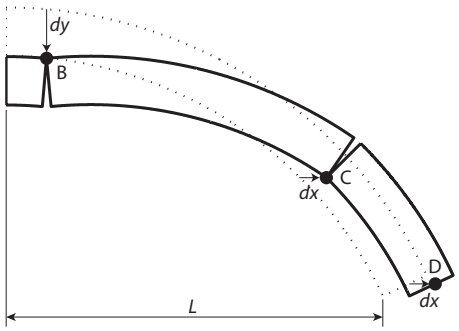

Figure 3.5: Schematic of hinge locations and displacement of arch.

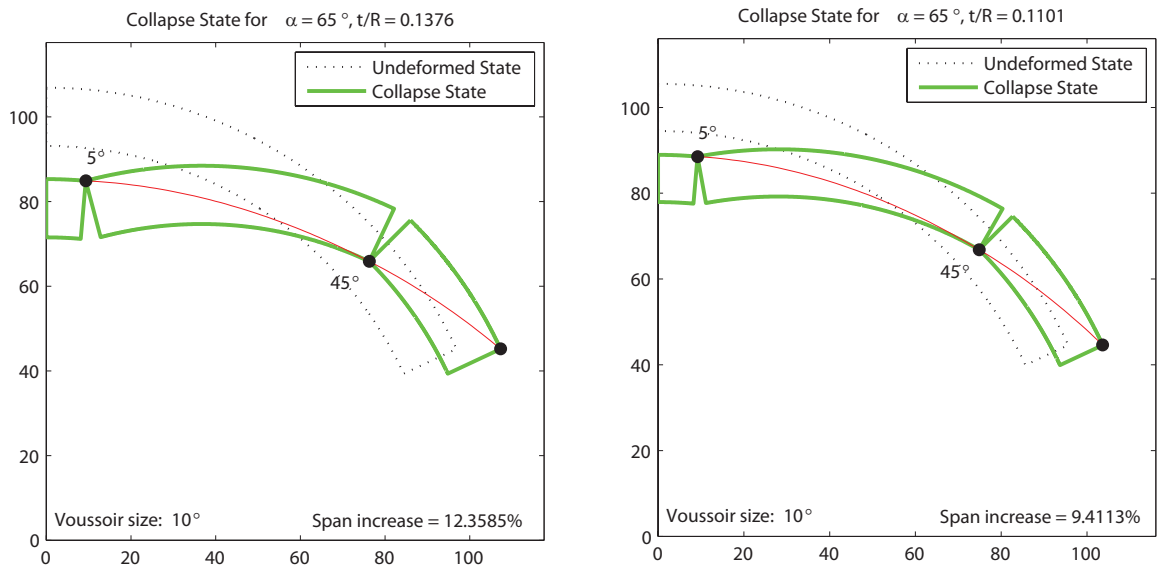

(a) (b)

Figure 3.6: BarrelSpread results for a 130° arch of (a) full thickness and (b) effective thickness of 80%. The predicted increases are 12.4% and 9.4%, respectively.

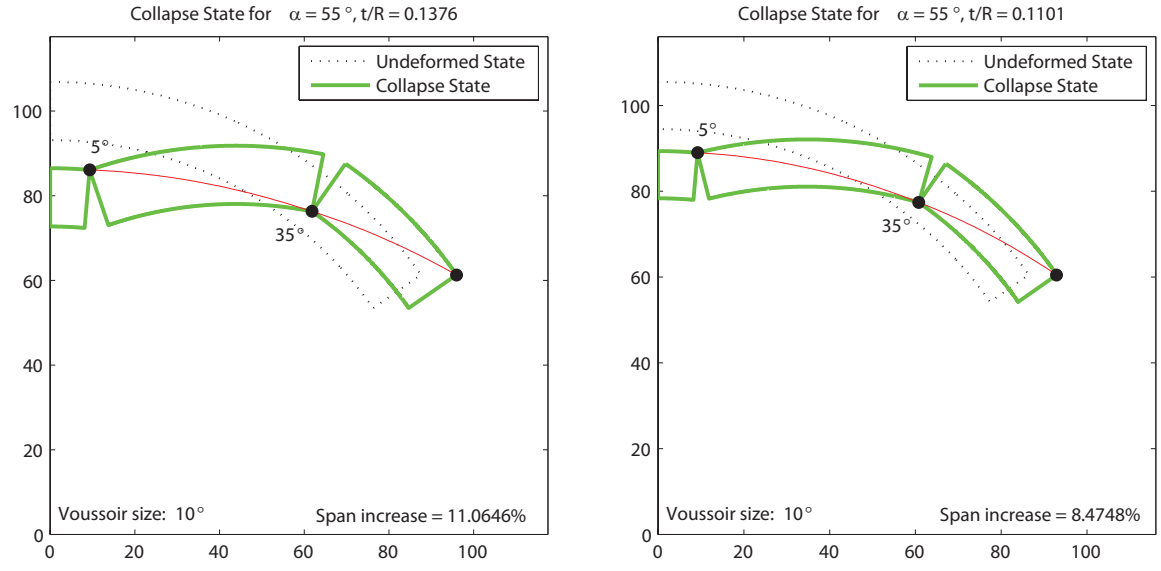

(a) (b)

Figure 3.7: BarrelSpread results for a 110° arch of (a) full thickness and (b) effective thickness of 80%. The predicted increases are 11.1% and 8.5%, respectively.

3.3 Discussion

The experimental, InteractiveThrust, and Matlab results are summarized in Figure 3.8. The experimental results of the groin vault and barrel vault of the same size differ by only

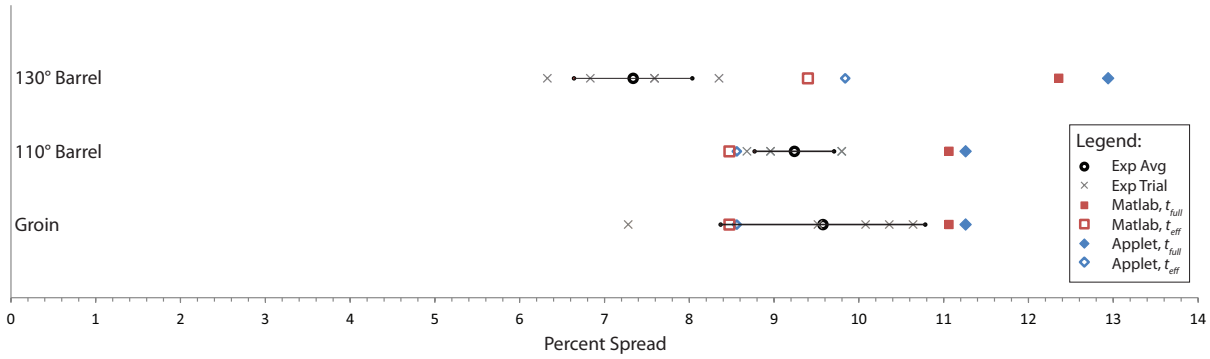

Figure 3.8: Summary of experimental, InteractiveThrust, and BarrelSpread results. Each experimental trial result is noted by a gray "x" and the experimental average is highlighted by a black circle with bars representing one standard deviation. BarrelSpread results are squares and InteractiveThrust results are diamonds. The full thickness is represented by a solid marker for each and the effective thickness by an open marker.

3%. The 130° barrel vault had a lower span increase than the 110° vault even though the opposite was predicted.

Overall, estimating the behavior of all the vaults as arches is a good method because the hinging patterns of each vault follow that of an arch. In all experimental trials, the hinges formed along a single, straight line for the entire depth of the vault.

There are several differences between the experiment and the geometry represented in each analytical approximation. First, the model has an odd number of evenly sized voussoirs, resulting in one block being centered at the crown of the arch. The InteractiveThrust applet assumes that the arch will hinge at the crown. In reality, the thrust line passes very close to the extrados at the crown, which allows hinges to begin opening on both sides of the central voussoir. Eventually, one hinge snaps closed due to slight imperfections in construction. This behavior is confirmed in the high-speed video footage. BarrelSpread more accurately represents the behavior of the vault by allowing the hinge at the crown to form at an angle of one half of a voussoir from the center.

Another difference is introduced by the method of input for the geometry in each approximation. BarrelSpread allows the exact geometry of the arch to be used for the calculations. The applet has discrete jumps in the thickness ratio (t/r) and abutment displacement that depend on the sensitivity of the user controlling particular points of the geometry displayed on the screen.

Finally, BarrelSpread determines the collapse geometry through a series of checks that the thrust line remains within the geometry of the arch. The applet allows the user to deform the arch in any manner and does not indicate valid or invalid results. It is the user's

responsibility to establish whether a given thrust line is stable or not and where the intrados hinge should be placed.

A major finding of these experiments is that the capacity of a groin vault to deform due to spreading is dominated by its constituent barrel vault that is spreading. The groin vault can be analyzed as two barrel vaults. The vault whose abutments are moving apart forms an extrados hinge near the crown and an intrados hinge along the haunches of the arch. The open ends of the second barrel begin to tilt upwards. In some experiments, a linear crack, approximately tracing the edge of the first vault, forms (Figure 3.2). The dominant behavior of the groin vault is that of the first barrel, so the estimation of the capacity of the groin vault can be done by analyzing an arch of the same angle of embrace and voussoir size.

Both the applet and Matlab program produce safe estimates for the 110° barrel vault and groin vault. It should be noted that the 130° barrel vault have unexpectedly low experimental results. Both analytical methods predict a span increase 11% greater than the 110° arch. However, the average experimental result is 20% lower. This discrepancy can be accounted for by the greater opportunity for construction errors introduced when the arch is made up of 13 blocks instead of 11. With more blocks, there are more opportunities for dynamic instabilities to occur. While care was taken to minimize any disturbances, some vibration is introduced by the rotation of the threaded rod required to move the abutment. Additionally, both methods analyze the arches as three rigid links, which significantly reduces the number of degrees of freedom from that of the scale model and reduces the sensitivity of the analysis to dynamic effects.

The behavior observed in the groin vault mirrors that shown by Van Mele et al. (2012) when one of the four supports is lowered in their study. The groins remain intact and several blocks fall out near the crown, revealing areas where compressive forces are not being transferred.

3.4 Summary

Experiments are done on three-dimensional printed vaults of three different geometries: 130° barrel vault, 110° barrel vault, and a groin vault made up of two 110° barrel vaults crossing at a right angle. These experiments are compared to two simplified approximations: a publicly available online applet and a Matlab program presented in this thesis. Both approximations assume that the vaults deform as a very deep arch, hinging in a linear manner.

The method of approximating vaults as arches resulted in reliable estimates for the 110° barrel vault and groin vault. By using an effective thickness of 80% of the full thickness, safe estimates are established for the spreading capacity. If a 110° barrel vault spanning five

meters experiences a span increase of 2%, the support moves 10 cm. This may seem like a significant increase visually, but it is still well below (at least four times) any predictions of collapse. Another significant finding is the capacity of the groin vault can be estimated as that of a barrel vault with the same angle of embrace. Next, the load capacity of undeformed vaults is examined.

Chapter 4

Point loads imposed on vaults

Other than bridges, historical masonry vaults are less likely to experience singular point loads than spreading supports. However, these loads can provide insight into the response of vaults to extreme load cases. In many tools, uniform loads such as self-weight are discretized as point loads to simplify the analysis process. Vertical point loads applied to barrel and groin vaults are discussed in this chapter.

4.1 Experimental Results

Point loads are applied at four points along the center of the depth of the 130° barrel vault (Figure 4.1). Point A is at the crown of the vault and the following points move towards the abutment by 20% of the half-span. A similar loading pattern is used for the groin vault. Loads are applied at the same spacing along the crown of one arm plus a fifth point at the edge of the crossing arm (Figure 4.2).

As the barrel vault is loaded, a three hinge mechanism begins to form. However, instead of hinging evenly through the depth of the vault, only one block is activated at the point of application, then, with each row moving away from the load, another block hinges and a triangular pattern of activated blocks forms. Figure 4.3 shows the progression of hinging from the front of the vault. First, the vault is undeformed (part a). When it is partially deformed, the blocks along the center of the depth begin to hinge, but the blocks at the edge of the vault are not activated by the thrust and show no hinging (part b). Finally, the collapse mechanism forms with the four hinges propagating to the edge of the vault (part c).

The load capacity for each vault and load location is summarized in Table 4.1. The barrel vault has the highest capacity when loaded at the crown. The load capacity decreases as the point of application moves towards the quarter span and then increases slightly as it reaches point D. The groin vault capacity remains fairly constant at the center three points, then increases at points D and E, which are closer to the open end of the arm.

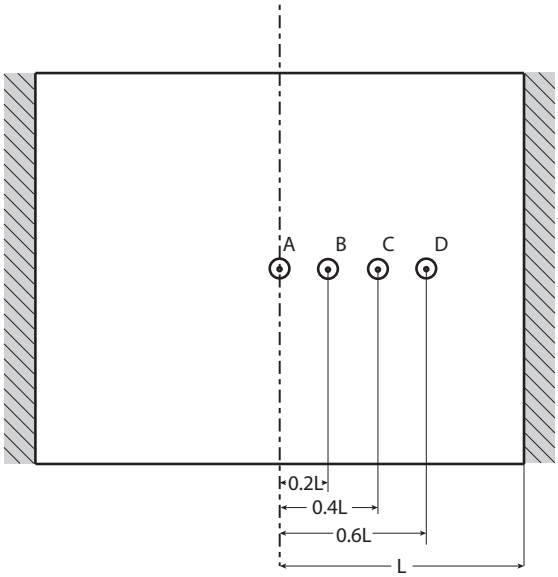

Figure 4.1: Point loads are applied at four locations along the barrel vault. They are centered in the depth of the barrel.

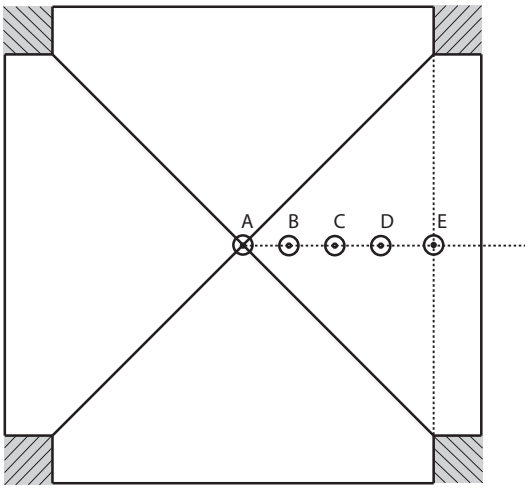

Figure 4.2: Point loads are applied at four locations along one arm of the groin vault following the spacing (20% of half-span) used for the barrel vault plus a fifth point located at the theoretical intersection of the crossing vault with the line of loads.

Table 4.1: Maximum load carried by the barrel and groin vault at each location

	Barrel [N]	Groin [N]
A	15.2	16.6
B	12.8	14.2
C	9.70	18.7
D	11.5	32.1
E	N/A	90.0

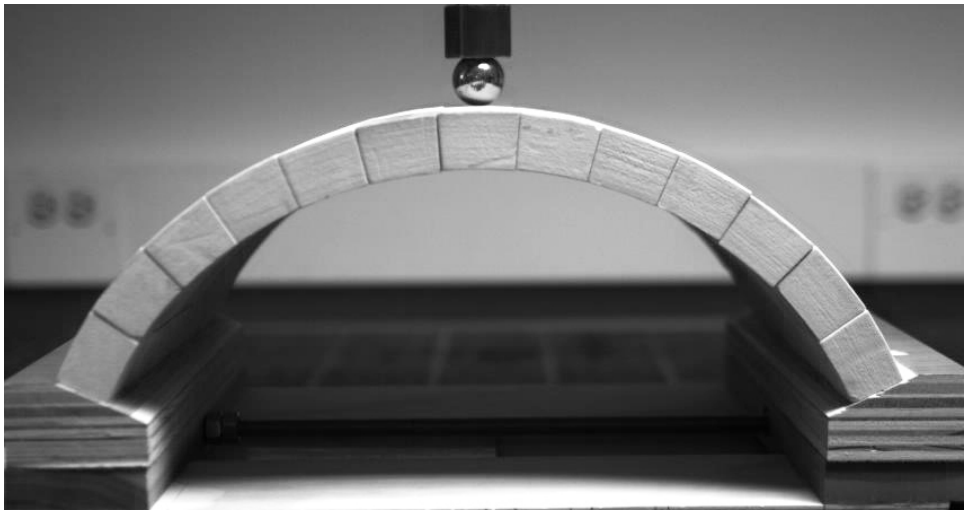

(a)

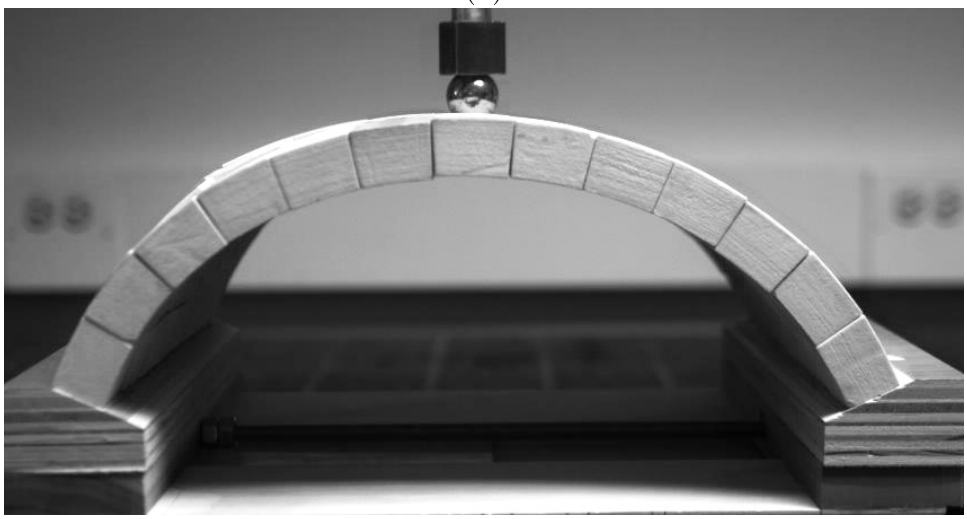

(b)

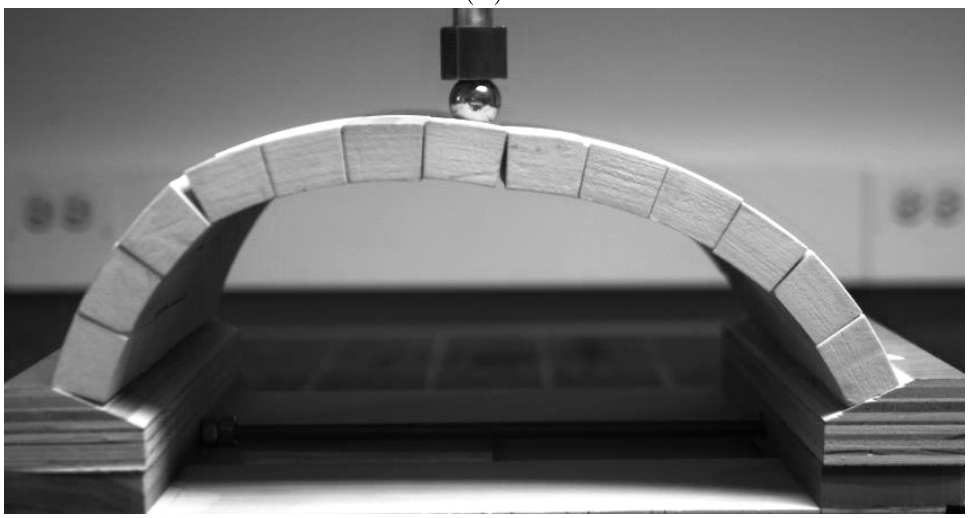

(c)

Figure 4.3: Still frames from high-speed footage of barrel loaded at midspan. Shown is (a) the undeformed vault, (b) the initial bulge to left of load, and (c) four hinges at collapse.

4.2 Analytical Results

Several analysis methods are developed to predict the capacity of the barrel and groin vaults. Each is based on thrust line analysis of a two-dimensional arch.

Arches collapse when a four-hinge mechanism forms. When an external point load is applied, the location of three of the hinges can be predicted. The natural shape of the thrust line under self-weight is a smooth curve that can vary within the masonry based on how much horizontal thrust is applied (Figure 4.4.a). When a point load is applied, the thrust line begins to straighten on either side of the load. To remain within the arch, the ends of the thrust line move towards the corners of the end blocks and three hinges form (Figure 4.4.b). The fourth hinge forms when the thrust line touches the intrados. Depending on the location of the load and the geometry of the arch, the intrados hinge near the abutment may move up the leg of the arch so that the fourth hinge can form (Figure 4.4.c)

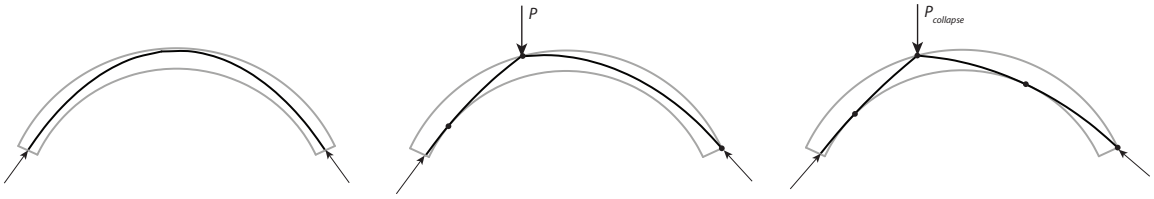

Figure 4.4: Shape of thrust line under (a) self-weight, (b) addition of a single point load less than collapse capacity, and (c) addition of a point load at collapse capacity with shifted intrados hinge. Hinges are identified by dots.

4.2.1 Collapse load Excel program

An automated program is developed in Excel to calculate the thrust line as well as horizontal and vertical reactions of an arch when the geometry of the arch, self-weight, and applied point loads are given. The user increases the external load until a solution is found where the thrust line sits just within the masonry, indicating the collapse load. Each time the load is increased, a check is made that the radius of the thrust line location is greater than the inner radius.

Once the geometry is entered, the program calculates the horizontal and vertical reactions by solving three simultaneous equations (4.1-4.3): two from global equilibrium (Figure 4.5.a), and one from a local equilibrium of the left hand side of the arch contained between the abutment and applied load (Figure 4.5.b). The program assumes that three of the hinge locations are known: the intrados of the abutment closest to the point load, the extrados at

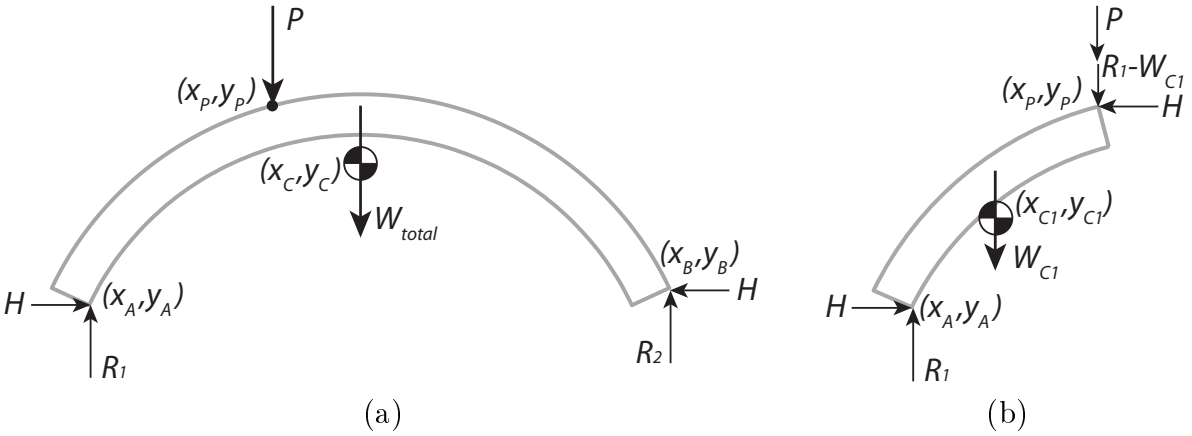

Figure 4.5: Forces and dimensions for (a) global and (b) local equilibrium equations.

the point of load application, and the extrados of the opposite abutment. Therefore, only one more hinge location must be found along the intrados between the two extrados hinges.

$$\sum M_P = 0 = -R_1 (x_P - x_A) + R_2 (x_B - x_P) + H (y_B - y_A) - W_{total} (x_C - x_P) \tag{4.1}$$

$$\sum F_y = 0 = R_1 + R_2 - P - W_{total} \tag{4.2}$$

$$\sum M_P = 0 = -R_1 (x_P - x_A) + H (y_P - y_A) - W_{C1} (x_P - x_{C1}) \tag{4.3}$$

Next, the thrust line is built in two pieces, each of which start at an abutment and meet at the point of load application. This is done by solving for the local equilibrium at each space between blocks (Eq. 4.4, Figure 4.6).

$$\sum M_A = 0 = -W_C (x_C - x_A) - (R_1 - W_C) (x_n - x_A) + H (y_n - y_A) \tag{4.4}$$

where

$$x_n = r_n sin\theta_n \tag{4.5}$$

$$y_n = r_n cos\theta_n \tag{4.6}$$

Variations of this program are used in the following three analyses with minor modifications to adapt to the parameters of each.

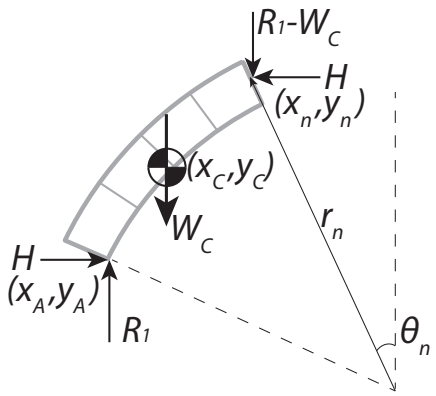

Figure 4.6: Forces and dimensions used to solve for the location of compression forces in a segment to build the thrust line.

4.2.2 Uniform depth arch analysis

A simplified approach to assessing the capacity of a barrel vault is to analyze it as a two-dimensional arch of uniform depth. Depending on the depth of arch selected, this method can either greatly underestimate or overestimate the capacity of the vault because the amount of material that is assumed to move changes, which affects the energy required for the collapse mechanism to form. This method was applied to the barrel vault of 130° for a slice of the vault that is one block thick (32 mm) and for the entire depth (254 mm). The two results provide a maximum and minimum for the capacity of the vault. The calculations are repeated using an 80% effective thickness.

Table 4.2: Arch analysis results for 130° barrel vault ($t/r = 14\%$)

Load Location	Capacity [N]			
	Single block (32 mm)		Full vault (254 mm)	
	t	$t_{eff} = 0.8t$	t	$t_{eff} = 0.8t$
A	5.9	3.1	46.7	24.8
B	4.1	2.6	32.6	20.5
C	4.1	2.6	32.6	20.5
D	4.2	2.8	33.4	22.6

4.2.3 Varied depth approximation

A second approximation of the vault capacity stems from the idea that when a point load is applied to a barrel vault, the force can radiate outward towards the abutment instead of in a straight line square to the arch (Figure 4.7.a). To simulate this capacity using the Excel program, it was assumed that each row of blocks incorporates one more block, effectively

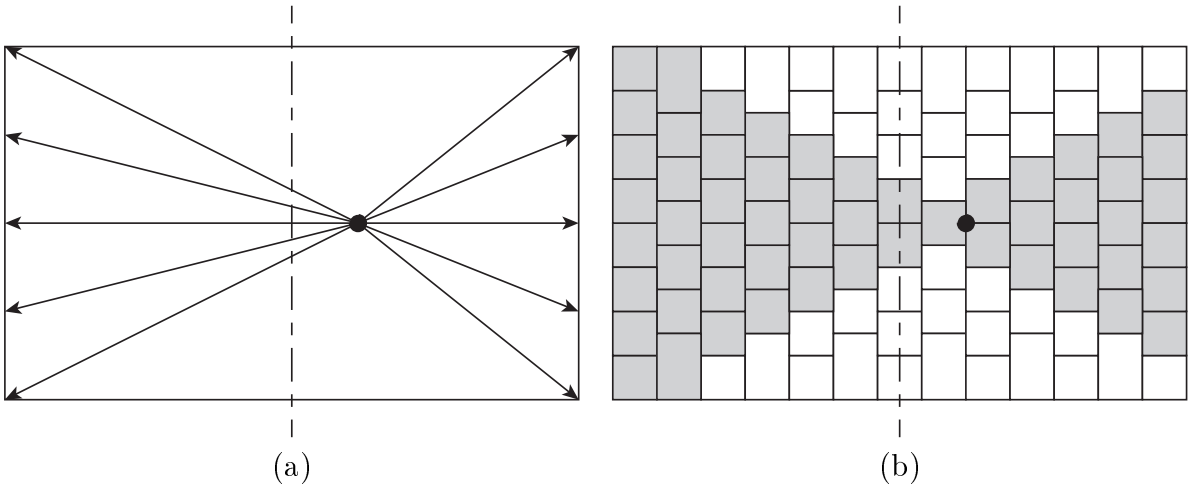

Figure 4.7: (a) When a point load is applied to a barrel vault (at the dot), the force paths can radiate outwards as they approach the abutment. (b) This idea can be translated to the barrel vault discretely by incorporating one more block width in each row moving away from the loaded point as shown by shaded blocks.

Table 4.3: Summary of Excel results for the varied depth approximation of 130° barrel vault capacity. ($t/r = 14\%$)

Load Location	Capacity [N]	
	t	$t_{eff} = 0.8t$
A	50.1	29.8
B	30.0	20.8
C	30.0	20.8
D	33.5	24.8

making each successive block heavier (Figure 4.7.b).

The pattern of activated blocks is the same for loads at A, B, and C with the load being applied as shown in Figure 4.7.b for B and C and one block to the left for point A. Point D shifts the triangles of activated blocks by one row, making the small triangle smaller and activating more blocks around the large triangle. The results are summarized in Table 4.3.

4.2.4 Superimposed crossing arches

To expand upon the idea of the force paths radiating out from the loaded point, the combined capacity of three crossing arches is estimated. One arch spans across the center of the depth of the vault and two more cross from corner to corner (Figure 4.8.a). Each arch is assumed to be one block (32 mm) deep. The two crossing arches are elliptical because they are an angled slice of the barrel vault. The principles of circular arches can be applied to elliptical ones. The Excel program was edited to include the irregular angles and centroids of the blocks in the elliptical arch. The circular arch has a capacity of 5.9 N and one elliptical

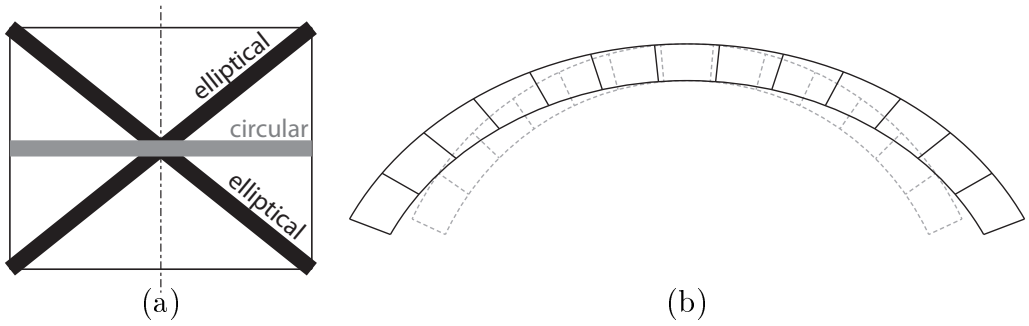

Figure 4.8: The barrel vault capacity can be estimated by superimposing three arches on the geometry of the vault. Arch position and geometry are shown in (a) plan and (b) cross-section.

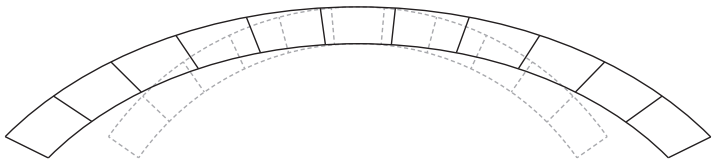

Figure 4.9: The elliptical arch along the groins of the cross fault varies only slightly from the circular arch of the cross-section of the vault.

arch can carry 4.9 N. So, together the estimated capacity is 15.6 N. By using an effective thickness of 80%, the total capacity reduces to 6.9 N (3.1 for the circular and 1.9 N for each elliptical arch), which represents a 56% reduction in capacity.

The capacity of the groin vault is more involved to calculate because of its intricate geometry. The capacity at the center can be estimated by summing the load capacity of the elliptical arches formed along the groins. Because the vaults cross at right angles, the groins are a 45° slice across the barrels. The elliptical arch varies only slightly from the circular one (Figure 4.9). The representative thickness of the elliptical arch is set to 32 mm based on the geometry of the blocks. The capacity of one elliptical arch is 18.1 N, so the estimated capacity of the groin vault is 36.2 N. Using an effective thickness of 80%, the calculated total groin vault capacity is reduced to 10.7 N.

4.3 Discussion

The average experimental results along with the four analytical predictions for the barrel vault are summarized in Table 4.4 and Figure 4.10. The groin vault average experimental results are summarized in Table 4.5 along with the crossing arch approximation for a load applied at the center of the vault.

Table 4.4: Summary of experimental and analytical results for a vertical point load applied at four locations along a 130° barrel vault. ($t/r = 14\%$)

Load Location	Experimental Average	Single Arch		Full Depth Arch		Varied Depth		Crossing Arches	
		t	t_{eff}	t	t_{eff}	t	t_{eff}	t	t_{eff}
A	15.2	5.9	3.1	46.7	24.8	50.1	29.8	15.6	9.2
B	12.8	4.1	2.6	32.6	20.5	30.0	20.8	—	—
C	9.7	4.1	2.6	32.6	20.5	30.0	20.8	—	—
D	11.5	4.2	2.8	33.4	22.6	33.5	24.8	—	—

Table 4.5: Summary of experimental and analytical results for a vertical point load applied at five locations along a 110° groin vault. ($t/r = 14\%$)

Load Location	Experimental Average	Crossing Arches	
		t	t_{eff}
A	16.6	36.2	10.7
B	14.2	—	—
C	18.7	—	—
D	32.1	—	—
E	90.0	—	—

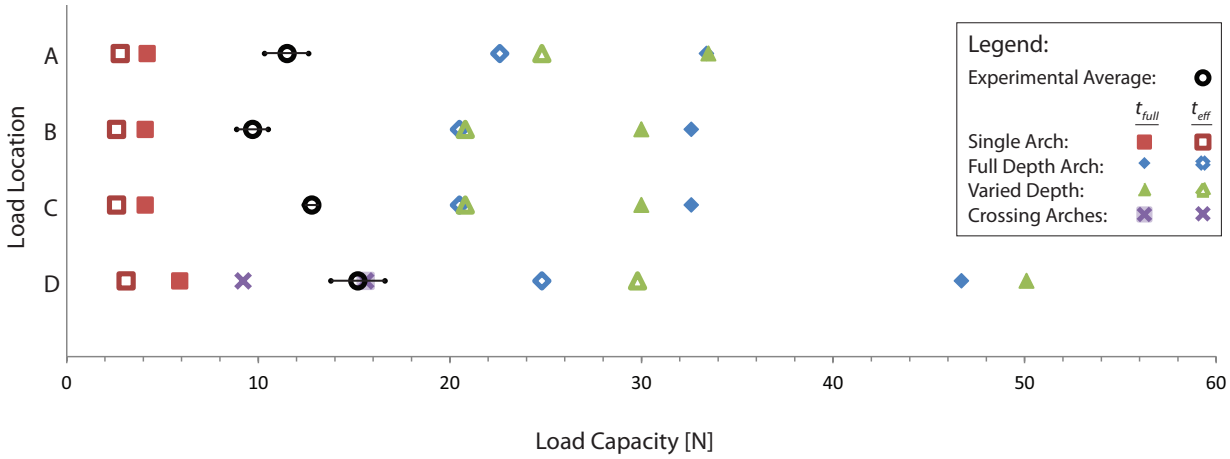

Figure 4.10: Summary of experimental and analytical results for a vertical point load applied at four locations along a 130° barrel vault ($t/r = 14\%$). The experimental average is highlighted by a black circle with bars representing one standard deviation. For each method, the full thickness is represented by a solid marker for each and the effective thickness by an open marker.

4.3.1 Barrel vault

The experimental results and analysis display a similar overall pattern in the capacity of the vault. The vault can support the greatest load when it is applied at the midspan. This

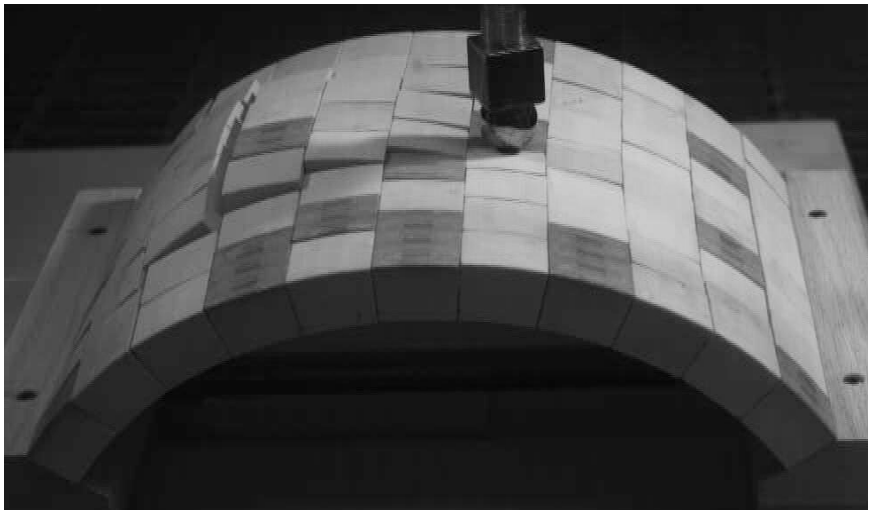

Figure 4.11: Triangular hinging of 110° barrel vault.

follows arch theory. As the load moves towards points B and C, the capacity decreases. This is because point C is very close to the quarter point, which is the weakest point of the arch. Finally, point D supports slightly more than point C because it is past the quarter point and closer to the abutment, so the load has a more direct path to the stable support.

The experimental results show that vaults do indeed have a higher capacity than a 2D arch of the same geometry. The hinging pattern in the scale model test show one or two blocks being activated in the rows closest to the point of load application and more blocks being included with each row moving towards the abutments. This triangular shape suggests the force path radiates outwards as it moves away from the load. Although it is not studied extensively here, the barrel vault with an angle of embrace of 110° displays the unique hinging behavior of the barrel form quite well (Figure 4.11). The blocks at the edges of the vault remain largely unaffected in the rows closest to the load application, while hinges form at the center of the depth. The selective movement of blocks reveals which ones are supporting the additional compressive force of the applied point load.

The first analytical approximation of estimating the vault as an arch with single blocks of various thickness is a crude representation of the vault behavior. When a depth of one block is used, the results are two to three times less than the experimental results. When the full depth of the vault is used, the capacity is overestimated by about three times. The depth could be calibrated to come up with a safe estimate of the capacity, but this brute force method may not be extensible to other geometries. While applying the idea of effective thickness lowers the full depth approximation, it is still too high to be useful.

The varied depth approximation yields a result that is higher than the single arch full depth approximation. At first pass, this may seem counter-intuitive given that varying

the depth of each row of blocks results in a lower overall mass than using the full depth. However, by concentrating the mass of the arch towards the abutments, as is done in the varied depth approximation, the thrust line of the unloaded arch is steeper than an arch with evenly distributed mass. Therefore, a higher external load is necessary to change the geometry of the thrust line so that it approaches the edge of the masonry. In a physical sense, this behavior indicates that more energy is required to move blocks that are closer to the haunches than to the crown of the vault. The method overestimates the capacity of the vault by three times using the full thickness and two times using the effective thickness, so it is not a useful tool for engineers assessing the capacity of existing masonry vaults.

The most successful estimation is the crossing arches method. By estimating the barrel vault as one circular and two elliptical arches crossing at the center of the span, the possible pathways for the force to transfer to the abutments are better represented than with a single arch. This analytical model represents each of the arches as one block deep and predicts the vault capacity to be 15.6 N, which is a 2% overestimates of the experimental result. By using the effective thickness, the model suggests a capacity of 9.2 N, which is 60% of the experimental average. This could be an acceptable safe limit for predicting the capacity of the vault with a generous factor of safety built in.

4.3.2 Groin vault

Testing on the groin vault is done with the pairs of groin blocks fixed to each other to best represent the actual construction of groin vaults. The experimental results show a fairly stable load capacity of the vault for points A, B, and C, which are centralized on the vault (Etlin 2011). The capacity of points D and E increase significantly. It is likely that the results of point E are skewed because of the particular geometry of the constituent barrel vaults. The thickness and angle of embrace of each vault allow straight lines to be drawn from a load applied at midspan to the abutments. Because the line is straight, the load can increase infinitely without changing shape and will therefore never pass out of the masonry. Since point E is applied so close to the edge of one of the arms of the groin vault, the theoretical infinite capacity of the arch is increasing the capacity in a way that is not possible in vaults without this same geometrical property.

Because of its complex geometry, estimating the capacity of the groin vault analytically is a difficult task. It is reasonable to assume that a load applied to the center of the span will be carried to the abutments in the most direct way possible, which is along the groin. The groins take the form of elliptical arches because the vault is an intersection of two barrels at a right angle. Using effective thickness, the crossing arches method suggests a capacity of

64% of the experimental average. Just as with the three crossing arches for the barrel vault, this method produces an acceptable safe limit for predicting the capacity of the vault. More accurate upper bound methods are needed to quantify the collapse capacity of groin vaults, but that is beyond the scope of this work.

4.4 Summary

The barrel and groin vault are subjected to vertical point loads applied to the exterior of the vault. The barrel vault capacity is at a maximum when loaded at the center of the span, decreases as the loaded point moves towards quarter span, and increases again slightly after passing the quarter point. The groin vault shows a fairly uniform capacity when loaded towards the center and a much higher capacity as the load moves towards the edge of an arm, but this behavior may be dominated by the particular geometry of the model vault.

An Excel program is created to estimate the capacity of the vault based on thrust line analysis. It is altered to accommodate three analysis methods: uniform depth arch analysis, varied depth approximation, and superimposed crossing arches. The uniform depth and varied depth analyses overestimate the capacity of the barrel vault and are therefore unsuccessful tools for assessing vaults. The superimposed crossing arches method provides a very safe lower bound estimate for both the barrel and groin vault when an effective thickness of 80% is used. In the next chapter, these results are extended to include the load capacity of initially deformed vaults.

Chapter 5

Load capacity of an initially deformed vault

It is common practice to estimate vault capacity based on perfect geometry, assuming exact construction and no changes to the structure during its lifetime. In reality, all structures suffer deformations over time due to factors such as foundation settlement, structural retrofits, and uneven loading. In this chapter, experiments on a model barrel vault and development of an accompanying analysis method are discussed. Two studies are done: one with the load applied at a single point while the initial deformation is varied and one with the load location varied for a single initial deformation.

5.1 Experimental Results

The 130° barrel vault is subjected to loading after an initial deformation is applied. Given the maximum spreading capacity established in Chapter 3, values for 25%, 50%, and 75% deformation are determined. The vault is constructed as normal, the abutments are spread to the desired deformation, then a load is applied. Figure 5.1 shows the progression of hinging and collapse as the vault is loaded in the center. Triangular hinging regions begin to form on either side of the load and eventually the hinges spread across the entire depth of the vault. The hinges snap between adjacent rows as the thrust line adjusts to hold the forces within the masonry. In each test, the final hinging pattern includes a hinge near the point of load application. The vault collapses when a hinge forms at the extrados of the vault at an abutment.

First, an in depth study is done for the vault loaded at midspan with each initial displacement. The results are summarized in Figure 5.2. Next, the maximum capacity for the vault with initial deformation of 50% and loads applied at points B, C, and D is tested. The aver-

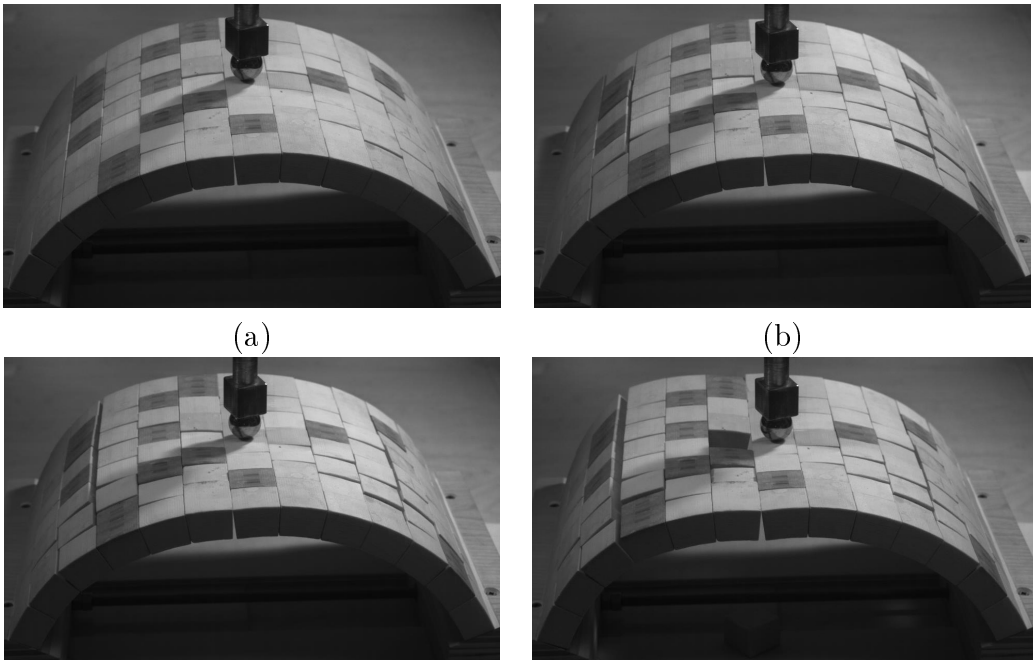

Figure 5.1: Still frames from high-speed footage of load testing of 130° barrel vault when initially deformed 25% of maximum spreading capacity. Progression of collapse is shown from (a) unloaded position to (d) collapse state.

age results are shown in Figure 5.3 along with the maximum load capacity for an undeformed vault in order to see the trends. The full trial results can be found in Appendix B.3.

5.2 Analytical Results - Matlab simulation

DomeSpread presented in Chapter 3 and Zessin (2012) is used as a starting point to analyze the load-carrying capacity of an arch that is initially deformed. The code, BarrelSpread+Load solves the maximum spread an arch can sustain, then calculates the geometry if the spreading is instead stopped at 25, 50, or 75% of the maximum. The user inputs the angle of embrace, thickness ratio, number of blocks in the arch, and final intrados hinge location. The load is simulated by increasing the weight of a one degree segment of the arch directly to the right of the extrados hinge at the crown. The horizontal thrust in the arch is recalculated each time the load is increased by solving the local equilibrium of the middle segment of the arch. With the updated horizontal force, the thrust line can be calculated for the entire arch. The results for a one block deep (32 mm) arch of full thickness and effective thickness of 80% are shown in Figures 5.4 and 5.5, respectively. The full Matlab function of BarrelSpread+Load can be found in Appendix C.2.

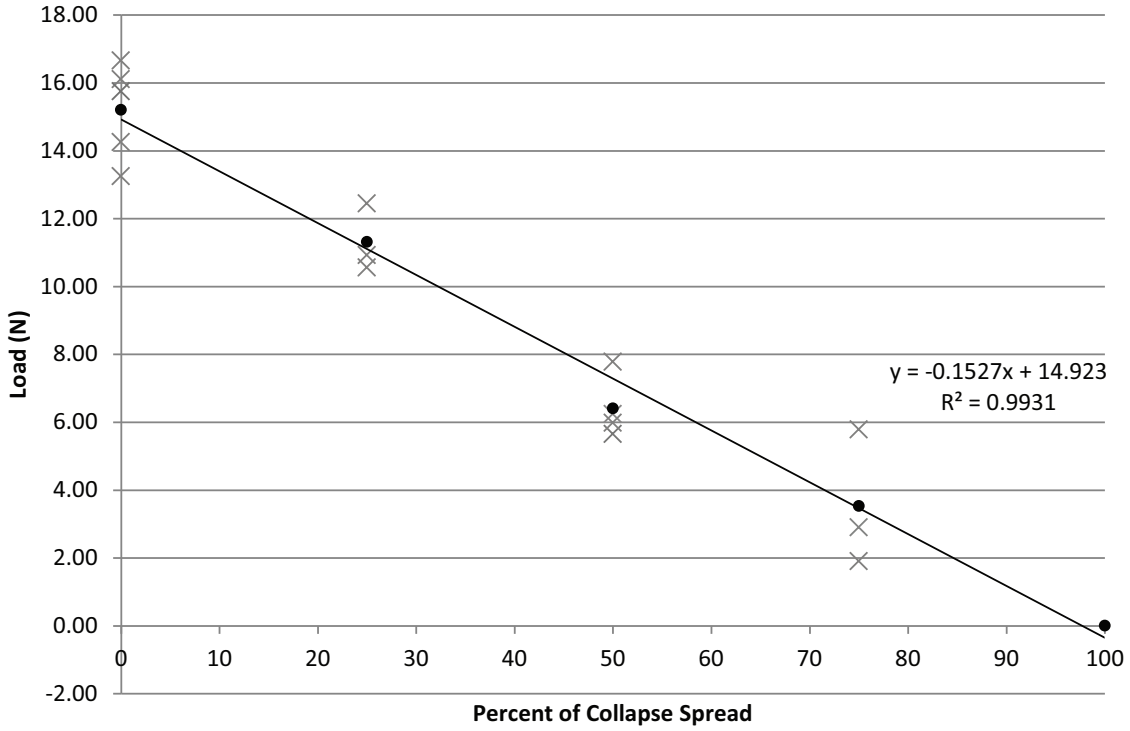

Figure 5.2: Trial and average results (marked with an X and dot, respectively) for 130° barrel vault ($t/r = 14\%$) loaded at midspan with initial deformations of 0, 25, 50, and 75% maximum abutment spread.

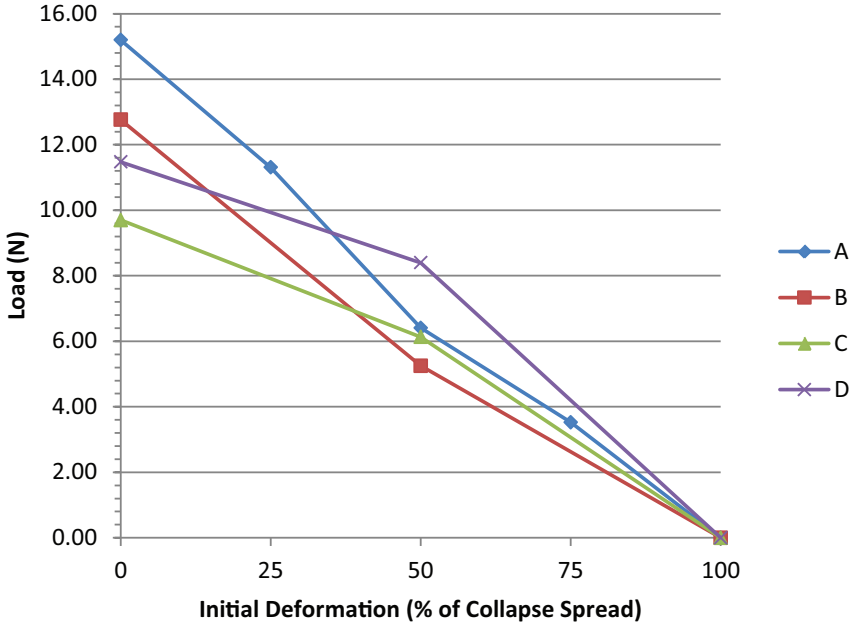

Figure 5.3: Average experimental results for 130° barrel vault ($t/r = 14\%$) loaded at midspan with initial deformations of 0, 25, 50, and 75% applied before loading at four points along mid depth.

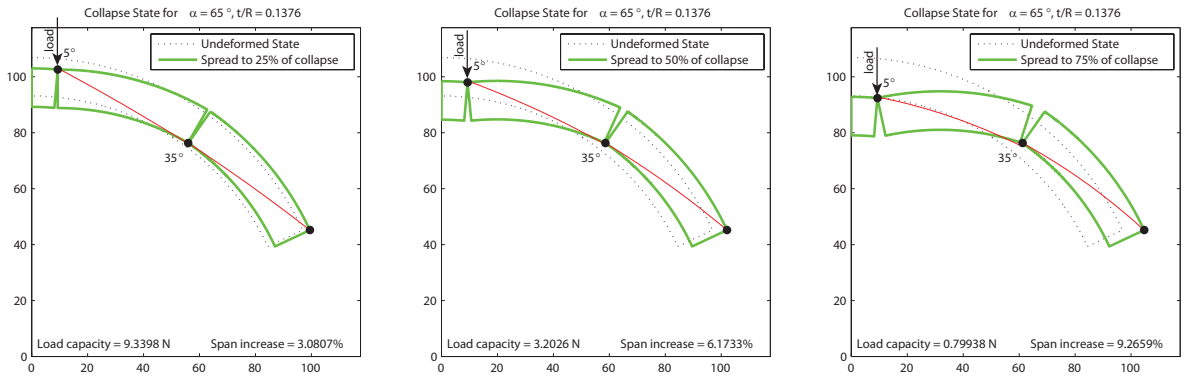

(a) (b) (c)

Figure 5.4: BarrelSpread+Load estimation of arch load capacity when arch has initial deformation of (a) 25%, (b) 50%, and (c) 75% of maximum spreading. Load capacity prediction is 9.3, 3.2, and 0.8 N, respectively. Estimation assumes arch is one block (32 mm) deep and has full thickness.

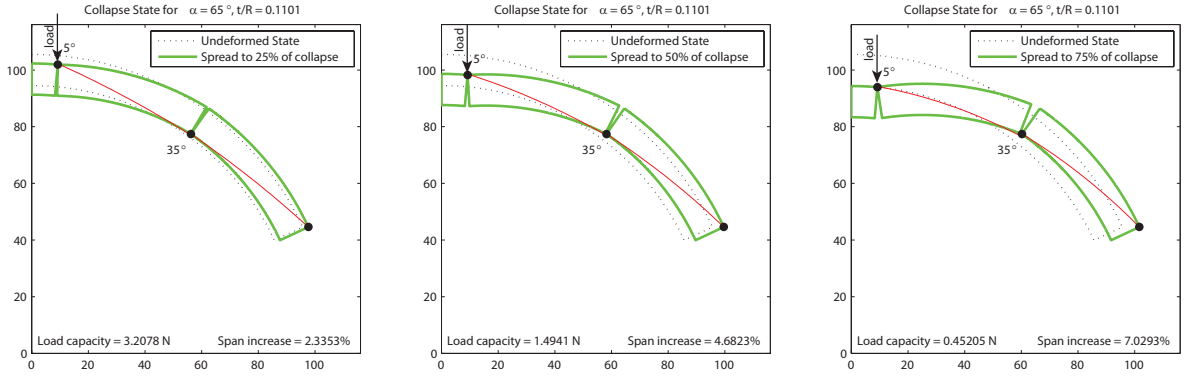

(a) (b) (c)

Figure 5.5: BarrelSpread+Load estimation of arch load capacity when arch has initial deformation of (a) 25%, (b) 50%, and (c) 75% of maximum spreading. Load capacity prediction is 3.2, 1.4, and 0.5 N, respectively. Estimation assumes arch is one block (32 mm) deep and has an effective thickness of 80%.

5.3 Discussion

The experimental average and Matlab results are summarized in Figure 5.6. The experimental results are four times the predicted effective thickness results while the full thickness results are between the two.

When an initial deformation is applied to the barrel vault, hinges open to accommodate the shifting thrust line. Then, when a load is applied, the hinges must shift as the thrust line flattens to reflect the single load. This adds complexity to the problem of solving the

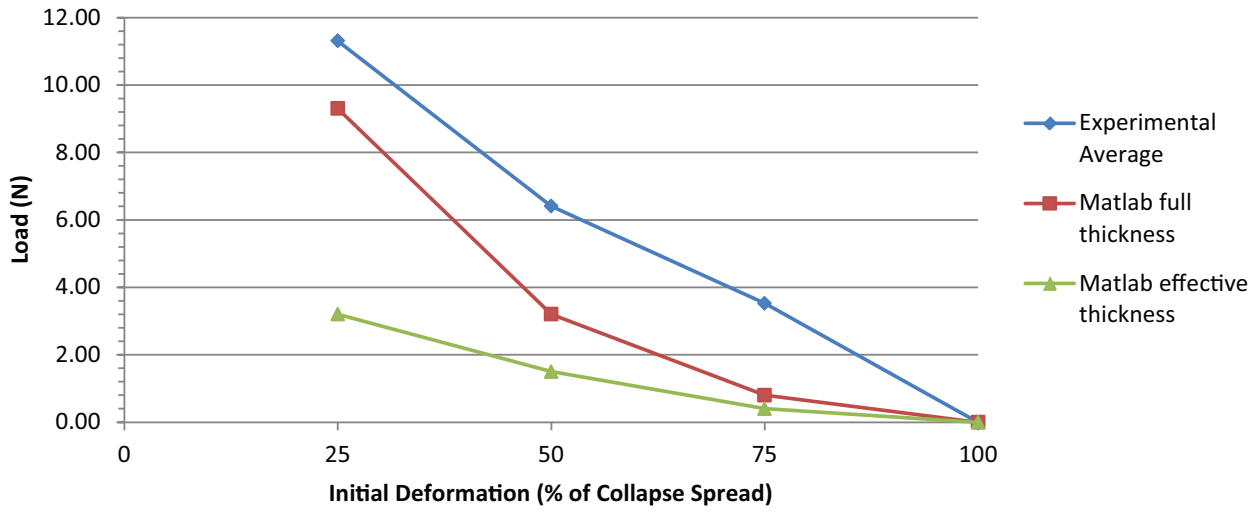

Figure 5.6: Experimental averages and Matlab predictions of load capacity of 130° barrel vault (t/r = 14%) loaded at midspan with initial deformations of 25, 50, and 75% applied before loading.

final collapse mechanism analytically.

In the experimental results, a linear relationship is displayed between the initial deformation (ranging from none to total collapse) and load carried. The averages for loading at point A follow a linear trend with R^2= 0.99. Trends for points B, C, and D are based on three data points, but seem to follow the linear trend that is established by more extensive testing at point A.

The BarrelSpread+Load approximations display a similar trend to that established experimentally. The experimental averages are three to four times greater than the effective thickness predictions. This mirrors the predictions for point loads on an undeformed vault discussed in Chapter 4. As established in Chapter 4, a single arch approximation does not accurately predict the capacity of the barrel vault. A more extensive study including methods to approximate the three-dimensional force paths of a vault would be the next steps.

The current simulation assumes symmetry about the center line of the vault. However, the thrust line is not symmetrical in the model studied because there is an uneven number of blocks. The thrust line approaches the shape of a "V" with the vertex at the point of load application. When there is a central voussoir (caused by an uneven number of blocks), the vertex shifts to one side so that a hinge can form, creating uneven legs. BarrelSpread+Load models only the shorter leg, causing the capacity to be slightly overestimated. The overestimation results in predictions that do not relate linearly to each other (Figure 5.6). Future work would extend the approximation to model the entire arch in order to more accurately predict the capacity.

5.4 Summary

In this chapter, point load experiments are performed on the 130° barrel vault with initial deformations imposed by spreading the supports. A Matlab program, BarrelSpread+Load, is also developed to predict the capacity of vaults of various geometries. The code predicts values that are significantly lower than the experimental results because the model is based on a single arch and does not account for the three-dimensional capacity of the barrel vault.

A major finding in this study is the linear relationship between load capacity and initial deformation. With this rule of thumb, engineers monitoring unreinforced masonry structures can estimate the remaining strength of a barrel vault given its capacity for loading, maximum span increase when undeformed, and the amount the supports have spread over time. Another major concern for the stability of historic masonry structures, earthquake loading, is explored in the next chapter.

Chapter 6

Lateral acceleration of vaults

Masonry vaults are found all over the world, including regions of high seismic activity. Unlike modern structures that are designed to meet strict seismic codes by absorbing energy through material deformation, vaults must continuously contain the thrust line within the geometry to remain stable.

The actual behavior of masonry structures under earthquake loads is complex and difficult to predict due to the rapidly changing location of the thrust line; a first-order approximation of horizontal acceleration can be achieved by tilting the structure. When the structure is tilted, gravity remains vertical, causing a local equilibrium on the structure with one component of gravity acting normal to the tilted surface and a second component acting parallel to the surface (Figure 6.1). Horizontal acceleration (α) is equal to the tangent of the angle of tilt (γ) multiplied by gravity.

6.1 Experimental Results

Testing is performed on two of the model vaults: the barrel vault with angle of embrace

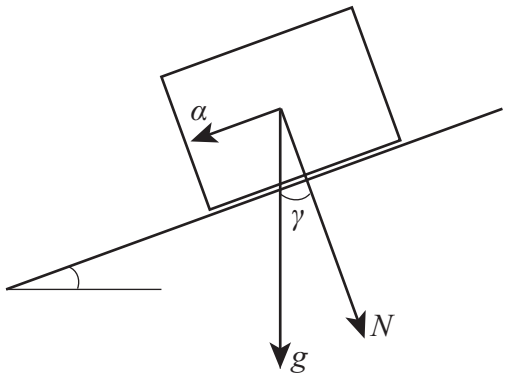

Figure 6.1: When tilted, a structure is locally subjected to a constant horizontal acceleration

130° and the groin vault. Each vault is tilted in multiple directions in order to establish the behavior of the vault under the wide range of accelerations experienced in an actual seismic event.

The barrel vault is tilted in three orientations. First with the abutments parallel to the axis of rotation, then perpendicular, and finally at a 45° angle (Figure 6.2). Each orientation allows for a different behavior to be observed. When the vault is tilted with the abutments parallel to the axis of rotation, the vault behaves as an arch, hinging linearly along the depth of the vault. This is reflective of the barrel vault behavior due to spreading. When the vault is tilted with the abutments perpendicular to the axis of rotation, a triangular section of the vault falls off with a combination of rotating and sliding. Finally, when the vault is tilted with the abutments at an angle to the axis of rotation, the vault hinges, but in a pattern that zigzags across the rows, not straight across as in the parallel test (Figure 6.3).

Next, the groin vault is tilted in two orientations (Figure 6.4). Testing on the groin vault is done with the pairs of groin blocks fixed to each other to best represent the actual construction of groin vaults. Given the symmetry of the vault, this is as extensive a survey as done for the barrel vault. When the vault is tilted in the parallel orientation, the constituent barrel whose abutments are parallel to the axis hinges as the single barrel does. The arms of the barrel that is perpendicular to the axis tilt in the same direction as the closest hinges. When the groin vault is tilted at a 45° angle, the elliptical arches clearly provide the most support for the vault. The groin that is perpendicular to the axis hinges in four locations as an arch is expected to. These hinges propagate through the arms of the vault (Figure 6.5).

The maximum horizontal acceleration sustained in each orientation for both vaults is summarized in Table 6.1. For full trial results see Appendix B.4.

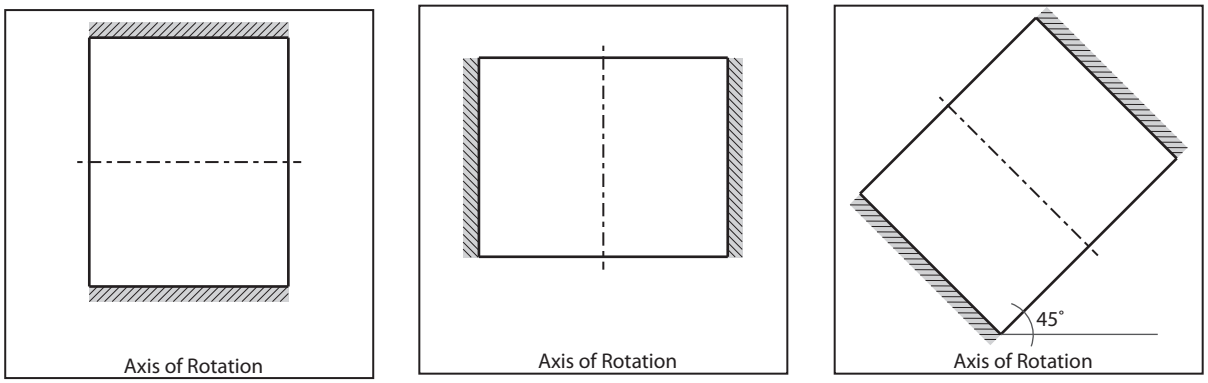

Figure 6.2: The barrel vault is tilted with the abutments (a) parallel, (b) perpendicular, and (c) 45° to the axis of rotation.

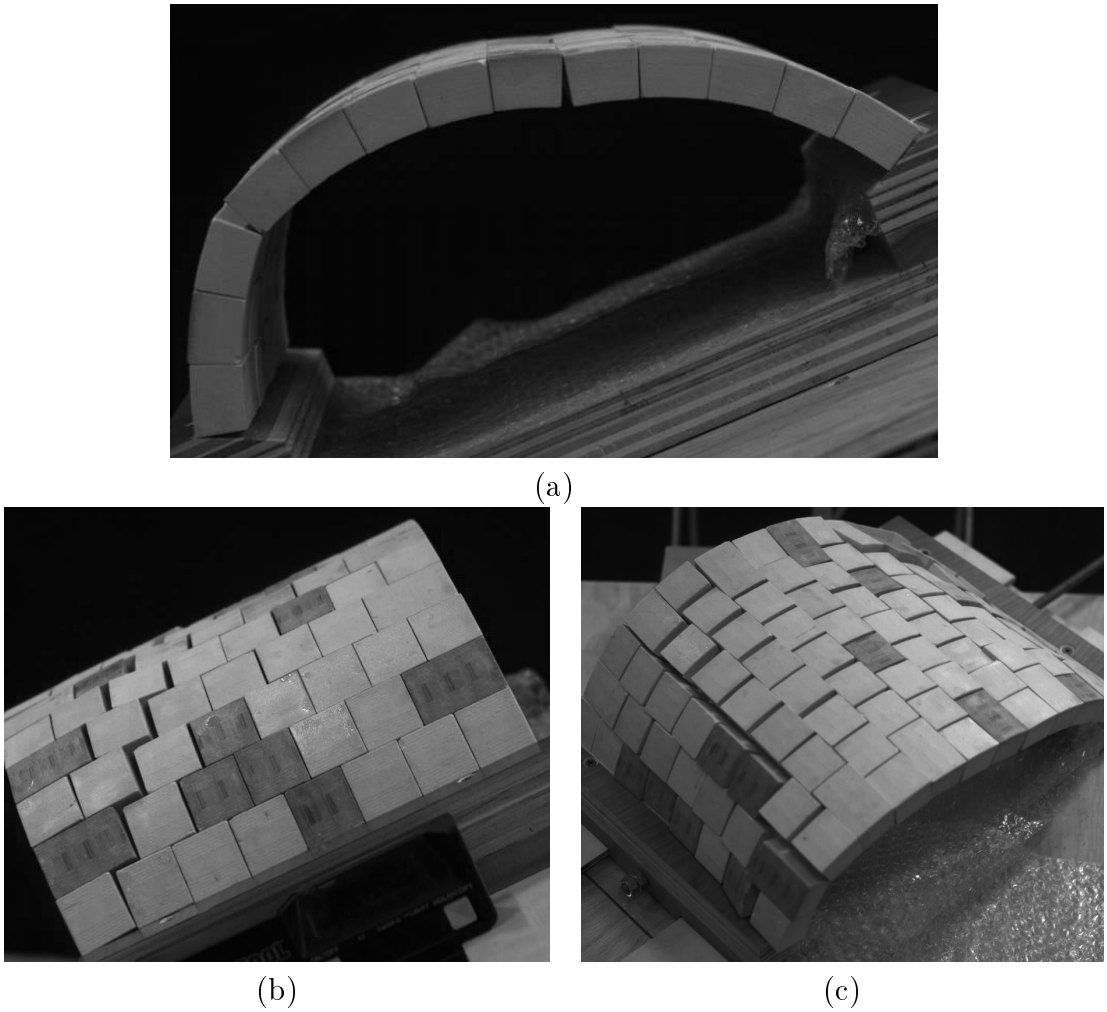

(a)

(b) (c)

Figure 6.3: Collapse mechanism of the barrel vault when subjected to tilting (a) parallel, (b) perpendicular, and (c) 45° to the axis of rotation.

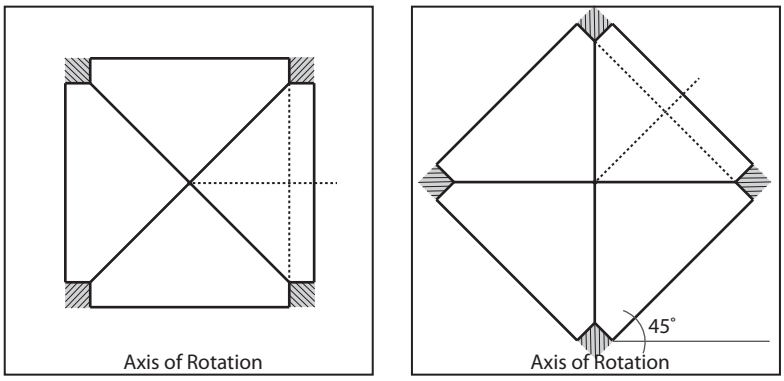

(a) (b)

Figure 6.4: The groin vault is tilted with the abutments (a) parallel, and (b) 45° to the axis of rotation.

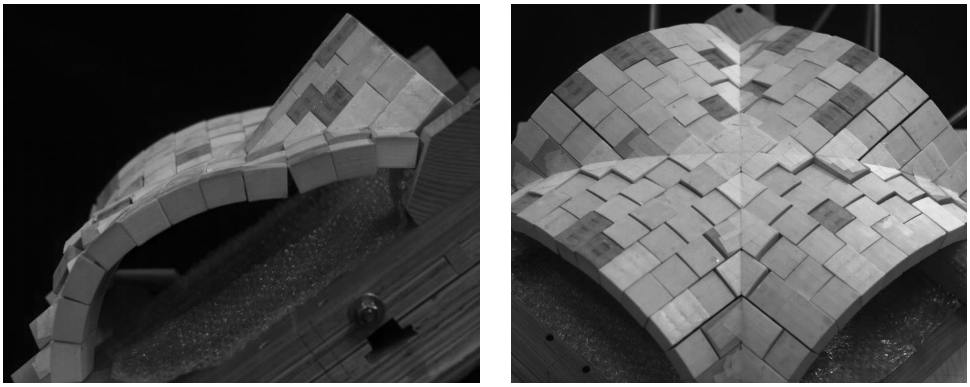

(a) (b)

Figure 6.5: Collapse mechanism of the groin vault when subjected to tilting (a) parallel and (b) 45° to the axis of rotation.

Table 6.1: Average experimental results from tilting test

Vault	Orientation	Angle	Horizontal Acceleration
Barrel	Parallel	24.2°	$0.45g$
	Perpendicular	27.6°	$0.52g$
	45°	30.5°	$0.59g$
Groin	Parallel	33.7°	$0.67g$
	45°	38.6°	$0.80g$

6.2 Analytical Results

Two methods are used to estimate the capacity of vaults when tilted in different directions. One is an online applet similar to that used to analyze spreading capacity of arches and the second is a calculation of centroid stability.

6.2.1 InteractiveThrust

An online applet called "Mechanism of Lateral Thrust" (DeJong 2010) estimates the lateral stability of an arch. This applet is used to estimate the capacities of the barrel and groin vaults when tilted with abutments parallel to the axis of rotation. Like the spreading applet, this lateral thrust applet requires the user to input the angle of embrace, thickness ratio, and adjust the angle of incline. The user can also manipulate the location of points A, B, and C along the thrust line. The results for the full and effective thickness of the 130° arch and 110° arch are shown in Figures 6.6 and 6.7.

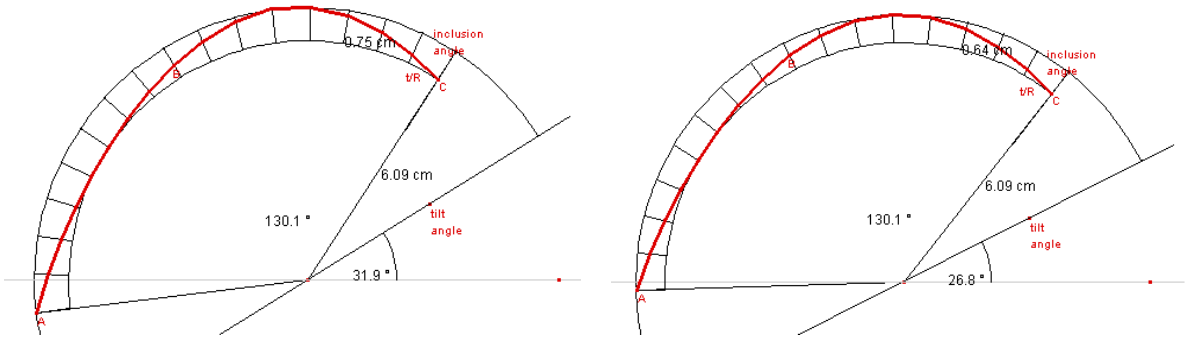

(a) (b)

Figure 6.6: InteractiveThrust results for a 130° arch (t/r = 14%) of (a) full thickness and (b) effective thickness of 80%. The predicted angles are 31.9° and 26.8°, respectively.

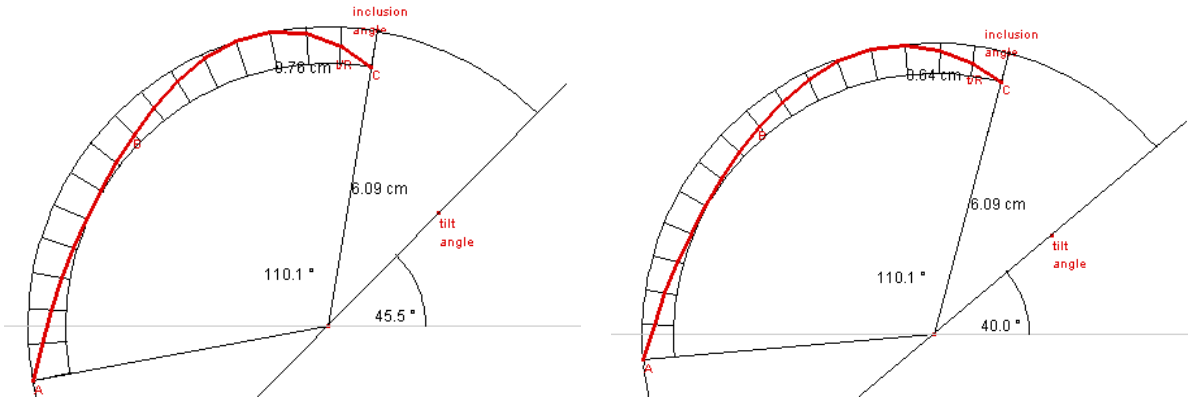

(a) (b)

Figure 6.7: InteractiveThrust results for a 110° arch (t/r = 14%) of (a) full thickness and (b) effective thickness of 80%. The predicted angles are 45.5° and 40.0°, respectively.

6.2.2 Centroid stability

When the vault is tilted with its abutments perpendicular to the axis of rotation, hinges do not easily develop because the blocks are staggered with respect to the direction of tilting.

Instead, the dominant failure mechanism is overturning. Therefore, to estimate the capacity of the vault, the centroid of a triangular portion is calculated and the angle of tilt before it passes outside of the supporting structure is calculated (Eq. 6.1, Figure 6.8).

$$tan\gamma = \frac{\bar{y}}{\bar{z}} \tag{6.1}$$

For the barrel vault, the angle of collapse is found to be 32.8°, which is equivalent to $0.65g$. It should be noted that the theory of effective thickness does not apply in this calculation because a thrust line is not being used.

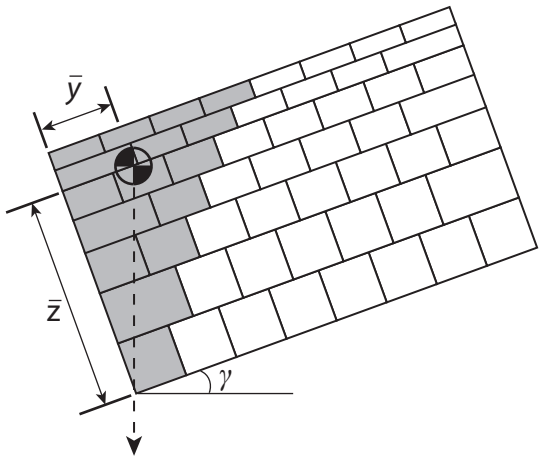

Figure 6.8: Elevation view of barrel vault with triangular section of blocks included in centroid calculation highlighted in gray and point of collapse when centroid is no longer supported by the structure after a rotation of γ.

6.3 Discussion

The experimental and analytical results for all horizontal acceleration tests are summarized in Figure 6.9 and Table 6.2.

The barrel vault, when tilted with its abutment parallel to the axis of rotation, behaves as an arch, hinging along the rows of blocks. The applet over predicts the capacity by 13% when an effective thickness of 80% is applied. Although care was taken to move the tilting platform as smoothly as possible, some vibrations from the motor may have caused collapse to occur sooner than predicted.

Table 6.2: Summary of experimental and analytical results for tilting tests including γ= angle of tilt and α= horizontal acceleration.

Vault	Orientation	Experimental Average		InteractiveThrust t		InteractiveThrust t_{eff}		Centroid Stability	
		γ		γ		γ		γ	
Barrel	Parallel	24.2°	$(0.45g)$	31.9°	$(0.62g)$	26.8°	$(0.51g)$	—	—
	Perpendicular	27.6°	$(0.52g)$	—	—	—	—	32.8°	$(0.65g)$
	45°	30.5°	$(0.59g)$	—	—	—	—	—	—
Groin	Parallel	33.7°	$(0.67g)$	45.5°	$(1.02g)$	40.0°	$(0.84g)$	—	—
	45°	38.6°	$(0.80g)$	—	—	—	—	—	—

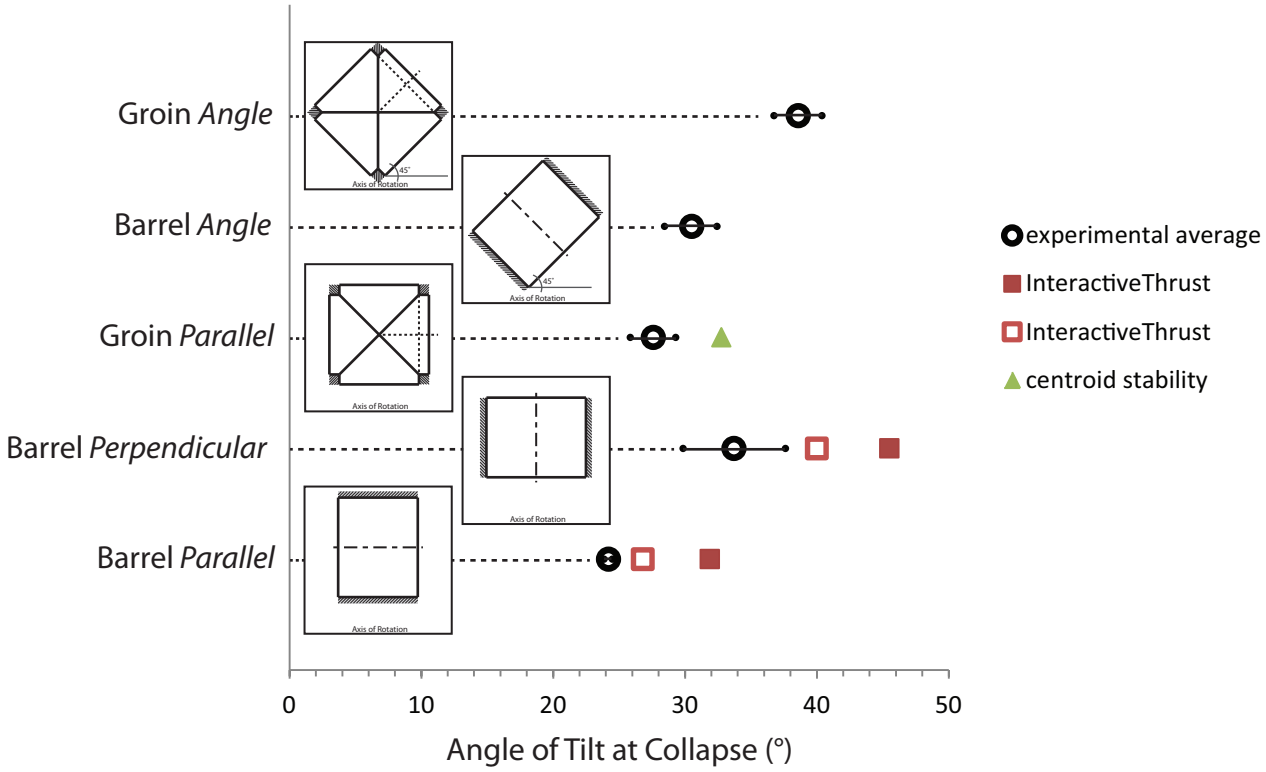

Figure 6.9: Summary of experimental and analytical results for tilting tests. The experimental average is highlighted by a black circle with bars representing one standard deviation. InteractiveThrust results are squares and the centroid stability result is a triangle. The full thickness is represented by a solid marker for each and the effective thickness by an open marker.

The method of centroid stability overestimates the actual collapse by 20%. This can be attributed to some blocks sliding before overturning occurs. Friction tests were performed to establish that the average coefficient of friction between two blocks is 0.44. This allows the blocks to develop an angle of 23° before sliding. The centroid calculation is based on

the observed overturning of the blocks in the experiment, but additional overturning planes could be considered to better predict the capacity of this orientation.

Future work would include assessing lateral stability of elliptical arches. This would be useful for predicting the capacity of the groin vault tilted at an angle to the axis of rotation because it appeared that the arch along the groin controlled the capacity of the vault. Also, the analysis of elliptical arches may be helpful in predicting the capacity of the barrel vault when tilted at an angle.

6.4 Summary

Tilting tests can be used as a first order approximation of earthquake loads by applying a constant horizontal acceleration to a structure. In this chapter, experiments on the 130° barrel vault and groin vault are discussed. Both vaults are tilted with the abutments parallel, perpendicular, and 45° to the axis of rotation and the angle of tilt is recorded, which can then be converted to a constant horizontal acceleration. Two analytical methods are presented to begin to explain the behavior. First, an online applet is used to predict the behavior of the vaults when the dominant failure mechanism mirrors that of an arch. The applet overestimates the capacity of the both vaults. Second, centroid stability is considered for the portion of the barrel vault that is subject to overturning. This method overestimates the capacity of the vault slightly as well. A contributing factor to this is the maximum angle of tilt of the blocks is less than the predicted angle. Future work in this area would include the stability of elliptical arches under lateral loading so that the capacity of barrel vaults and groin vaults tilted an an able to the axis of rotation can be predicted.

Chapter 7

Conclusions

This thesis presents results from four major areas: spreading supports, point loads, loading of an initially deformed vault, and lateral acceleration. Each area is supported with experimental results from scale model testing and simplified analytical approximations. Scale model experiments can give great insight into the performance of full-scale structures at very low cost. Fabrication and construction costs are orders of magnitude lower than full-scale models. Three-dimensional printing allows for any shape to be built without need for a skilled mason. Additionally, they can be reused for multiple experiments, increasing their cost effectiveness further. These experiments should be considered as useful tools for practicing engineers to examine the stability of a vault and how close it is to a collapse mechanism.

While the scale models may reveal details that can disappear in the assumptions of mathematical models and suggest the true three-dimensional behavior of vaults, the simplified analytical models provide a more accessible route for engineers to evaluate structures. The models presented in this thesis allow for a wide range of geometrical parameters to be used as inputs and results to be presented with a basic understanding of vault behavior on the part of the user.

7.1 Investigation review

First, the spreading capacity of a vault is examined. Experimentally, it was found that groin vaults have a span increase capacity equal to the constituent barrel vault that is being spread. This makes estimating the span increase capacity very straightforward. Barrel vaults can be analyzed as arches with very deep voussoirs because the hinges form linearly along the rows of blocks. A two-dimensional arch approximation estimates the capacity nicely. This thesis presents a Matlab program, called BarrelSpread, for predicting the span increase, which does an effective job.

Second, the point load capacity of a barrel and groin vault is investigated. The experiments reveal hinging patterns that suggest the force paths in barrel vaults radiate outwards from the point of load application to the abutments. This informs the creation of analytical approximations. Four methods are presented in Chapter 4. The most accurate assumes the load capacity is equal to that of three superimposed arches: one circular one at the center depth and two crossing diagonally from opposite corners. Using an effective thickness of 80%, this method predicts the capacity within 40% of the experimental results. By using this method, engineers can establish a safe, lower limit estimation.

The third investigation looks for a trend between the first two limits already established: maximum span increase and maximum load capacity. Through extensive experimental testing of the barrel vault loaded at midspan, it is determined that load capacity decreases linearly with initial deformation. That is to say, a 25% initial deformation reduces the load capacity by 25%. A Matlab program, called BarrelSpread + Load, is presented, which determines the geometry of the partially deformed vault and then increases the applied load until the thrust line can no longer be held within the vault. It is a good first step in analyzing the capacity of a deformed vault with a point load; however, it does not include the three-dimensional load paths as the analysis loads on a perfect vault did. And so, future work will include the extension of this analysis. This investigation is potentially the most useful for engineers evaluating existing structures. Most current analysis is based around perfect geometry, but structures in use have suffered deformations over time and therefore have a different geometry. This analytical model is a strong first step in providing engineers with a tool to assess the capacity of vaults that have suffered deformations.

The fourth and final investigation is a look at the stability of vaults when exposed to the lateral accelerations of earthquakes. As a first-order approximation, the model vaults are tilted, which causes a component of gravity to apply constant horizontal acceleration to the vault. The main result of this section is a thorough documentation of the collapse mechanisms of the barrel and groin vault that form when lateral acceleration is applied in different directions. high-speed footage records the final acceleration and mechanism at collapse of the structures. Simple analysis is done through use of an online applet and geometric calculations of the stability of sections to overturn. The footage can be used to inform more complex analysis in the future. Additionally, engineers examining vaults in the field can look for particular hinging patterns as signs of weakening due to horizontal acceleration.

Each of these investigations sheds light on the behavior of unreinforced masonry barrel and groin vaults. Several useful analytical approximations are introduced as new tools for engineers to establish safe lower bounds on the capacity of vaults. Additionally, the detailed

documentation through high-speed footage of model collapse provides insight to cracking patterns in existing structures that engineers can use to determine the stresses on a vault through observation.

7.2 Key findings

Several key conclusions can be drawn from the scale model experiments and simplified analytical models:

- As the supports of a barrel vault spread apart, it will hinge as if made up of very deep voussoirs. Therefore, it can be analyzed as a two-dimensional arch.
- The spreading capacity of a groin vault is governed by the constituent barrel that is spreading, so a two-dimensional arch analysis of the single barrel will provide an adequate estimation of maximum span increase.
- An effective method for estimating the capacity of a barrel vault to carry vertical point loads is three superimposed arches crossing at the point of load application.
- The capacity of a barrel vault decreases linearly with the initial support deformation.
- Tilting provides an effective first-order approximation for the behavior of vaults in response to earthquake loads.

7.3 Future work

The studies presented in this thesis have several logical extensions. Experiments can be carried out for more barrel geometries in order to create a firmer lower limit for the span increase capacity. Next, in the point load analysis, the crossing arch analysis can be expanded to include more load locations. Each new load position requires new arch geometries to be computed. Additionally, more accurate upper bound methods are needed to quantify the groin vault capacity. The three-dimensional models can be expanded to accommodate the initial deformation explored in Chapter 5 as the current models only examine two-dimensional behavior. Finally, there are many open questions regarding the behavior of vaults under earthquake loading. Investigations into the stability of elliptical arches with lateral accelerations can be applied to stability analysis of barrel and groin vaults tilted at an angle.

Appendix A

References

3D Systems (last accessed May 2012). `http://www.zcorp.com`.

Allen, E. and W. Zalewski (2010). *Form and Forces: Designing Efficient, Expressive Structures*. John Wiley & Sons.

Block, P., T. Ciblac, and J. Ochsendorf (2006). Real-time limit analysis of vaulted masonry buildings. *Computers and Sturctures 84*(29-30), 1841–1852.

Block, P., M. DeJong, and J. Ochsendorf (2006). As hangs the flexible line: Equilibrium of masonry arches. *Nexus Network Journal 8*(2), 12.

Block, P. and L. Lachauer (2012). Three-dimensional equilibrium analysis of gothic masonry vaults. In *8th International Conference on Structural Analysis of Historical Constructions*.

Block, P. and J. Ochsendorf (2007). Thrust newtork analysis: A new methodology for three-dimensional equilibrium. *Journal of the International Association for Shell and Spatial Structures 48*, 167–173.

Boothby, T. (2001). Analysis of masonry arches and vaults. *Progress in Structrual Engineering and Materials 3*, 246–256.

Clemente, P. (1998). Introduction to dynamics of stone arches. *Earthquake Engineering and Structural Dyamics 27*, 513–522.

De Lorenzis, L., M. DeJong, and J. Ochsendorf (2007). Failure of masonry arches under impulse base motion. *Earthquake Engineering and Structural Dyamics 36*, 2119–2136.

DeJong, M. (last modified September 2010). Dynamics of masonry arches: Mechanism of lateral failure. `http://www-civ.eng.cam.ac.uk/struct/mjd/arch_dynamics.html`.

DeJong, M., L. DeLorenzis, S. Adams, and J. Ochsendorf (2008, November). Rocking stability of masonry arches in seismic regions. *Earthquake Spectra 24*, 847–865.

DeJong, M. J. (2009, June). *Seismic Assessment Strategies for Masonry Structures*. Ph. D. thesis, Massachusetts Institute of Technology.

Etlin, R. (2011, July). Personal communication.

Heyman, J. (1982). *The Masonry Arch*. Horwood Limited.

Heyman, J. (1995). *The Stone Skeleton*. Cambridge, United Kingdom: Cambridge University Press.

Heyman, J. (1998). *Structural Analysis: A Historical Approach*. Cambidge, United Kingdom: Cambridge University Press.

Livesley, J. K. (1992). *A computational model for the limit analysis of three-dimensional masonry structures*, pp. 161–172. Boston: Kluwer Academic Publishers.

McNeel North America (last accessed May 2012). `http://www.rhino3d.com`.

MIT Masonry Research Group (last accessed May 2012a). `http://web.mit.edu/masonry`.

MIT Masonry Research Group (last accessed May 2012b). Arch collapse i. `http://web.mit.edu/masonry/interactiveThrust/applets/applet03.html`.

MIT Masonry Research Group (last accessed May 2012c). Interactivethrust: Semicircular arch. `http://web.mit.edu/masonry/interactiveThrust/examples.html`.

Ochsendorf, J. (2002). *Collapse of Masonry Structures*. Ph. D. thesis, University of Cambridge.

Ochsendorf, J. (2006). The masonry arch on spreading supports. *The Structural Engineer 84*(2), 29–35.

Ochsendorf, J. and A. Romano (2010). The mechanics of gothic masonry arches. *International Journal of Architectural Heritage 4*, 59–82.

O'Dwyer, D. (1999). Funicular analysis of masonry vaults. *Computers & Structures 73*(5), 187–197.

Pippard, A. J. S., E. Tranter, and L. Chitty (1936). The mechanics of the voussoir arch. *Journal of the ICE 4*, 281–306.

Quinonez, A., J. Zessin, A. Nutzel, and J. Ochsendorf (2010). Small-scale models for testing masonry structures. *Advanced materials Research 133-134*, 497–502.

Van Mele, T., J. McInerney, M. J. DeJong, and P. Block (2012). Physical and computational discrete modelling of masonry vault collapse. In *8th International Conference on Structural Analysis of Historical Constructions*.

Zessin, J. (2012). *Collapse analysis of unreinforced masonry domes and curving walls*. Ph. D. thesis, Massachusetts Institute of Technology.

Zessin, J., W. Lau, and J. Ochsendorf (2010). Equilibrium of cracked masonry domes. *Proceedings of the Institution of Civil Engineers - Engineering and Computational Mechanics 163*(163), 135–145.

Appendix B

Complete experimental results

B.1 Spreading tests

Trial	130° Barrel Vault	110° Barrel Vault	Groin Vault
1	21.4	25.4	27.0
2	23.8	27.8	28.6
3	26.2	27.8	20.6
4	19.8	25.4	30.2
5	23.8	24.6	29.4
Average	23.0 mm	26.1 mm	27.1 mm

B.2 Point load tests

Trial	Barrel Vault				Groin Vault				
	A	B	C	D	A	B	C	D	E
1	13.24	12.38	10.63	11.80	15.1	16.8	18.5	28.7	82
2	16.10	12.79	9.08	12.40	17.1	12.5	15.5	36.2	98
3	16.66	13.11	9.39	9.80	17.8	13.5	20.5	32.2	87
4	14.25	—	—	11.90	16.5	14.1	20.4	31.3	93
5	15.74	—	—	—					
Average	15.20	12.76	9.70	11.48	16.6	14.2	18.7	32.1	90

B.3 Point load on an initially deformed vault tests

B.3.1 Barrel vault loaded at midspan with 0, 25, 50, and 75% initial deformation

Trial	Initial Deformation			
	0%	25%	50%	75%
1	13.24	12.44	5.64	2.90
2	16.10	10.56	7.78	5.78
3	16.66	10.92	6.23	1.90
4	14.25	—	5.97	—
5	15.74	—	—	—
Average	15.20	11.31	6.41	3.53

B.3.2 Barrel vault loaded at mid depth with 50% initial deformation

Trial	Load Location			
	A	B	C	D
1	5.6	5.2	6.3	8.1
2	7.8	6.1	5.7	7.0
3	6.2	5.4	6.4	10.1
4	6.0	4.3	—	—
Average	6.4	5.3	6.1	8.4

B.4 Tilting tests

Trial	Barrel			Groin	
	Parallel	Perpendicular	45°	Parallel	45°
1	28.3	24.3	32.0	34.3	40.5
2	28.8	24.4	31.1	37.3	36.9
3	25.6	23.8	28.2	29.6	38.3
Average	27.6	24.2	30.4	33.7	38.6

Appendix C

Matlab Code

C.1 BarrelSpread

```
% Calculate minimum thrust and final collapse state for a spreading arch
% to replicate models: alpha=65/55, n=13/11, uncomment 'Force Hinges'
%                      t/r= .1376(full), .1101(t_eff)

%%%%%%%%%%%%%%%%%%%%%%%%%%%%%%%%%%%%%%%%%%%%%%%%%%%%%%%%%%%%%%%%%%%%%%%%%%%
% Adapted from function written by Jennifer Zessin and presented in: %
% Zessin, J. (2012). Collapse analysis of unreinforced masonry       %
% domes and curving walls . Ph.D. thesis, MIT.                       %
%%%%%%%%%%%%%%%%%%%%%%%%%%%%%%%%%%%%%%%%%%%%%%%%%%%%%%%%%%%%%%%%%%%%%%%%%%%

function [spread_final,dip_final,H_Hmin,hinges]  = ...
    barrel_spread (alpha,t_R,n,dx_start,figs)

close all;

fig1_title = ['Minimum Thrust State for \alpha = ',int2str(alpha),...
    '\circ, t/R = ',num2str(t_R)];
fig2_title = ['Collapse State for \alpha = ',int2str(alpha),...
    '\circ, t/R = ',num2str(t_R)];

%%%%%%%%%%%%%%%%%%%%%%%%%%%%%%%%%%%%%%%%%%%%%%%%%%%%%%%%%%%%%%%%%%%%%%%%%%%
% DETERMINE MIN THRUST STATE - NO SPREAD
[H_min,v_tot,hinges]  = barrel_min_thrust (alpha,t_R,n,figs);

intrados = hinges(2)*pi/180;
extrados = hinges(1)*pi/180;
```

```
27
28 %%% *** Force Hinges ***% for use when replicating model
29 intrados = 35*pi/180;
30 extrados = 5*pi/180;
31 %%%%%%%%%%%%%%%%%%%%%%%%%%%%%%%%%%%%%%%%%%%%%%%%%%%%%%%%%%%%%%%%%%%%%%%%%%%%
32
33 %%%%%%%%%%%%%%%%%%%%%%%%%%%%%%%%%%%%%%%%%%%%%%%%%%%%%%%%%%%%%%%%%%%%%%%%%%%%
34 % DEFINE GEOMETRY PARAMETERS
35 % embrace
36 alpha = alpha*pi/180;
37 % t and R properties
38 R = 100;
39 t = R*t_R;
40 ri = R-t/2;
41 ro = R+t/2;
42
43 %%%%%%%%%%%%%%%%%%%%%%%%%%%%%%%%%%%%%%%%%%%%%%%%%%%%%%%%%%%%%%%%%%%%%%%%%%%%
44 % DETERMINE VALID THRUST STATE - SPREADING
45
46 valid = 1;
47
48 % set precision of dx step
49 dx_precision = 1/100;
50 i = 1;
51 i_max = 0.8*R/dx_precision;
52
53 while (valid == 1) && (i < i_max)
54
55     valid = 0;
56
57     dx = dx_start + (i-1)*dx_precision;
58
59     %%%%%%%%%%%%%%%%%%%%%%%%%%%%%%%%%%%%%%%%%%%%%%%%%%%%%%%%%%%%%%%%%%%%%%%%%%%%
60     % DEFINE GEOMETRIC PARAMETERS
61
62     % points Bo,Co
63     Bo = ro*[sin(extrados), cos(extrados)];
64     Co = ri*[sin(intrados), cos(intrados)];
65
66     % define volumes vAB, vBC, vAC, vCD
67     % define center of gravity of BC and CD
68     % AB
69     [~,~,vAB] = segment_properties_EES(ri,ro,0,extrados);
```

```
70      % AC
71      [~,~,vAC] = segment_properties_EES(ri,ro,0,intrados);
72      % BC
73      [xBCo,yBCo,vBC] = segment_properties_EES(ri,ro,extrados,intrados);
74      % CD
75      [xCDo,~,vCD] = segment_properties_EES(ri,ro,intrados,alpha);
76      %%%%%%%%%%%%%%%%%%%%%%%%%%%%%%%%%%%%%%%%%%%%%%%%%%%%%%%%%%%%%%%%%%%%
77
78      % define points B, C, D {where B(2) and D(1), D(2) are unknown}
79      B = [Bo(1), 0];              %B only lowers, so Bx is constant
80      C = [Co(1)+dx, Co(2)];       %C moves right, so Cy is constant
81      D = [0, 0];                  %D can float along abutment as the abut
82                                   %moves right without rotation
83
84      % determine y displacement {length of BC is constant}
85      % syms dy
86      % dy = eval(solve('(Bo(1)-Co(1))^2+(Bo(2)-Co(2))^2=...
87          %(Bo(1)-Co(1)-dx)^2+(Bo(2)-dy-Co(2))^2', dy));
88      dy = Bo(2)-Co(2)-...
89          (2*dx*Bo(1)-2*dx*Co(1)+Bo(2)^2+Co(2)^2-dx^2-2*Bo(2)*Co(2))^(1/2)
            ;
90
91      % define B(2) {D(1) and D(2) still unknown}
92      B(2) = Bo(2)-dy;
93
94      % determine rotation of bar BC
95      rotBC = atan((Co(2)-Bo(2))/(Bo(1)-Co(1)))-atan((C(2)-B(2))/(B(1)-C
          (1)));
96      % determine new position of xBC,yBC
97      temp = rot_ccw([xBCo-Bo(1),yBCo-Bo(2)],rotBC);
98      xBC = B(1)+temp(1);
99
100     % determine thrust from equilibrium of BC
101     H = (vAC*(C(1)-B(1))-vBC*(xBC-B(1)))/(B(2)-C(2));
102
103     % determine rd -> D(1), D(2)
104     xCD = xCDo+dx;
105     rd = (vCD*(xCD-C(1))+H*C(2)+v_tot*(C(1)-dx))/...
106         (v_tot*sin(alpha)+H*cos(alpha));
107     D = [rd*sin(alpha)+dx, rd*cos(alpha)];
108
109     % check global equilibrium, by checking validity of rd
110     valid = range_check(0,ro*sin(alpha)+dx,D(1));
```

```
111
112     if valid == 1
113         H_increase(i) = H;
114         spread(i) = dx/(ri*sin(alpha));
115         dip(i) = dy/ri;
116         B_final = B;
117         C_final = C;
118         D_final = D;
119         rotBC_final = rotBC;
120         Co_final = Co;
121         vAB_final = vAB;
122         vAC_final = vAC;
123     else
124         mode = 'D is invalid';
125     end
126     i = i+1;
127 end
128
129 spread_final = spread(i-2)*100;
130 dx_final = spread(i-2)*(ri*sin(alpha));
131 dip_final = dip(i-2)*100;
132 dy_final = dip(i-2)*ri;
133 H_final = H_increase(i-2);
134 H_Hmin = H_increase(i-2)/H_min;
135
136
137 n=180;
138 %%%%%%%%%%%%%%%%%%%%%%%%%%%%%%%%%%%%%%%%%%%%%%%%%%%%%%%%%%%%%%%%%%%%%%%%%%%
139 % thrust in BC
140 % define x,y coordinates for thrust line
141 temp = rot_ccw(([0,-dy_final]-B_final),rotBC_final);
142 O = B_final+temp;
143
144 j_max = round(n*(intrados-extrados)/2/alpha);
145 xy2=zeros(j_max,2);
146 r=zeros(j_max,1);
147 for j = 1:j_max
148     phi2 = extrados+(intrados-extrados)/j_max*j;
149     [x_cg,y_cg,vol] = segment_properties_EES(ri,ro,extrados,phi2);
150     % calc rotated cg of segment Bb wrt O
151     temp = rot_ccw([x_cg,y_cg]-Bo,rotBC_final);
152     xBb = temp(1)+B_final(1)-O(1);
153
```

```
154     r(j) = (H_final*(B_final(2)-O(2))+vol*xBb+vAB_final*(B_final(1)-O(1)
          ))/...
155         ((vAB_final+vol)*sin(phi2-rotBC_final)+H_final*cos(phi2-
              rotBC_final));
156     xy2(j,:) = [r(j)*sin(phi2-rotBC_final)+O(1),r(j)*cos(phi2-
          rotBC_final)+O(2)];
157 end
158
159 % thrust in CD
160 j_max = round(n*(alpha-intrados)/2/alpha);
161 xy3=zeros(j_max,2);
162 r=zeros(j_max,1);
163 for j = 1:j_max
164     phi2 = intrados+(alpha-intrados)/j_max*j;
165     [x_cg,~,vol] = segment_properties_EES(ri,ro,intrados,phi2);
166
167     r(j) = (vol*(x_cg-Co_final(1))+H_final*Co_final(2)+(vAC_final+vol)
          *...
168         Co_final(1))/(H_final*cos(phi2)+(vAC_final+vol)*sin(phi2));
169     xy3(j,:) = [r(j)*sin(phi2)+dx_final,r(j)*cos(phi2)];
170 end
171 %%%%%%%%%%%%%%%%%%%%%%%%%%%%%%%%%%%%%%%%%%%%%%%%%%%%%%%%%%%%%%%%%%%%%%%%
172
173 if figs == 1
174     %%%%%%%%%%%%%%%%%%%%%%%%%%%%%%%%%%%%%%%%%%%%%%%%%%%%%%%%%%%%%%%%%%%
175     % PLOT DEFORMED GEOMETRY
176     barrel = segment_outline(ri,ro,pi/2,pi/2-alpha,0,0,0);
177     % AB
178     AB = segment_outline(ri,ro,pi/2,pi/2-extrados,0,-dy_final,0);
179     % CD
180     CD = segment_outline(ri,ro,pi/2-intrados,pi/2-alpha,dx_final,0,0);
181     % BC
182     BC = segment_outline(ri,ro,pi/2-extrados,pi/2-intrados,0,0,0);
183     temp = rot_ccw([BC(:,1)-Bo(1),BC(:,2)-Bo(2)],rotBC_final);
184     BC = [temp(:,1)+Bo(1),temp(:,2)+B_final(2)];
185
186     %plot
187     figure(2)
188     plot(barrel(:,1),barrel(:,2),'k:','LineWidth',1);
189     hold on;
190     plot(AB(:,1),AB(:,2),'g',BC(:,1),BC(:,2),'g',CD(:,1),CD(:,2),'g',...
191         'LineWidth',2);
192     hold on;
```

```
193     plot([B_final(1);xy2(:,1)],[B_final(2);xy2(:,2)],'r',...
194         [C_final(1);xy3(:,1)],[C_final(2);xy3(:,2)],'r');
195     hold on;
196     plot(D_final(1),D_final(2),'k.',C_final(1),C_final(2),'k.',...
197         B_final(1),B_final(2),'k.','MarkerSize',20);
198     axis equal;
199     axis([0 1.1*ro 0 1.1*ro]);
200
201     legend('Undeformed State','Collapse State');
202     title(fig2_title);
203
204     text(.97*ri,2,['Span increase = ',num2str(spread(i-2)*100),'%'],...
205         'VerticalAlignment','bottom','HorizontalAlignment','center','
              FontSize',10)
206     text(.97*C_final(1),.97*C_final(2),[int2str(intrados*180/pi),'\circ'
          ],...
207         'VerticalAlignment','top','HorizontalAlignment','right','
              FontSize',10)
208     text(1.03*B_final(1),1.03*B_final(2),[int2str(extrados*180/pi),'\
          circ'],...
209         'VerticalAlignment','bottom','HorizontalAlignment','left','
              FontSize',10)
210     text(2,2,['\it{Voissoir size: }',int2str(10),'\circ'],...
211         'VerticalAlignment','bottom','HorizontalAlignment','left','
              FontSize',10)
212 end
213
214 end
```

C.2 BarrelSpread+Load

```
% Calculate minimum thrust and final collapse load for an arch that has
% been spread to 25, 50, or 75% of collapse state and loaded at hinge
% to replicate models: alpha=65/55, n=13/11, uncomment 'Force Hinges'
%                      t/r= .1376(full), .1101(t_eff)

%%%%%%%%%%%%%%%%%%%%%%%%%%%%%%%%%%%%%%%%%%%%%%%%%%%%%%%%%%%%%%%%%%%%%%%%%%%
% Adapted from function written by Jennifer Zessin and presented in: %
% Zessin, J. (2012). Collapse analysis of unreinforced masonry       %
% domes and curving walls . Ph.D. thesis, MIT.                       %
%%%%%%%%%%%%%%%%%%%%%%%%%%%%%%%%%%%%%%%%%%%%%%%%%%%%%%%%%%%%%%%%%%%%%%%%%%%


function [spread_final,dip_final,H_Hmin,hinges]  = ...
    barrel_spread_load_fix (alpha,t_R,n,dx_start,position,figs)

close all;

fig1_title = ['Minimum Thrust State for \alpha = ',int2str(alpha),...
    '\circ, t/R = ',num2str(t_R)];
fig2_title = ['Collapse State for \alpha = ',int2str(alpha),...
    '\circ, t/R = ',num2str(t_R)];

%%%%%%%%%%%%%%%%%%%%%%%%%%%%%%%%%%%%%%%%%%%%%%%%%%%%%%%%%%%%%%%%%%%%%%%%%%%
% DETERMINE MIN THRUST STATE - NO SPREAD
[H_min,v_tot,hinges]  = barrel_min_thrust (alpha,t_R,n,figs);

intrados = hinges(2)*pi/180;
extrados = hinges(1)*pi/180;

%%% *** Force Hinges ***% for use when replicating model
intrados = 45*pi/180;
extrados = 5*pi/180;
%%%%%%%%%%%%%%%%%%%%%%%%%%%%%%%%%%%%%%%%%%%%%%%%%%%%%%%%%%%%%%%%%%%%%%%%%%%

%%%%%%%%%%%%%%%%%%%%%%%%%%%%%%%%%%%%%%%%%%%%%%%%%%%%%%%%%%%%%%%%%%%%%%%%%%%
% DEFINE GEOMETRY PARAMETERS
% embrace
alpha = alpha*pi/180;
% t and R properties
R = 100;
```

```
t = R*t_R;
ri = R-t/2;
ro = R+t/2;

%%%%%%%%%%%%%%%%%%%%%%%%%%%%%%%%%%%%%%%%%%%%%%%%%%%%%%%%%%%%%%%%%%%%%%%%%%%%
% DETERMINE VALID THRUST STATE - SPREADING

valid = 1;

% set precision of dx step
dx_precision = 1/100;
i = 1;
i_max = 0.8*R/dx_precision;

while (valid == 1) && (i < i_max)

    valid = 0;

    dx = dx_start + (i-1)*dx_precision;

    %%%%%%%%%%%%%%%%%%%%%%%%%%%%%%%%%%%%%%%%%%%%%%%%%%%%%%%%%%%%%%%%%%%%%%%%%%%%
    % DEFINE GEOMETRIC PARAMETERS

    % points Bo,Co
    Bo = ro*[sin(extrados), cos(extrados)];
    Co = ri*[sin(intrados), cos(intrados)];

    % define volumes vAB, vBC, vAC, vCD
    % define center of gravity of BC and CD
    % AB
    [~,~,vAB] = segment_properties_EES(ri,ro,0,extrados);
    % AC
    [~,~,vAC] = segment_properties_EES(ri,ro,0,intrados);
    % BC
    [xBCo,yBCo,vBC] = segment_properties_EES(ri,ro,extrados,intrados);
    % CD
    [xCDo,~,vCD] = segment_properties_EES(ri,ro,intrados,alpha);
    %%%%%%%%%%%%%%%%%%%%%%%%%%%%%%%%%%%%%%%%%%%%%%%%%%%%%%%%%%%%%%%%%%%%%%%%%%%%

    % define points B, C, D {where B(2) and D(1), D(2) are unknown}
    B = [Bo(1), 0];              %B only lowers, so Bx is constant
    C = [Co(1)+dx, Co(2)];       %C moves right, so Cy is constant
    D = [0, 0];                  %D can float along abutment as the
```

```
84                                  %abut moves right without rotation
85
86      % determine y displacement {length of BC is constant}
87      % syms dy
88      % dy = eval(solve('(Bo(1)-Co(1))^2+(Bo(2)-Co(2))^2=...
89          %(Bo(1)-Co(1)-dx)^2+(Bo(2)-dy-Co(2))^2', dy));
90      dy = Bo(2)-Co(2)-...
91          (2*dx*Bo(1)-2*dx*Co(1)+Bo(2)^2+Co(2)^2-dx^2-2*Bo(2)*Co(2))^(1/2)
              ;
92
93      % define B(2) {D(1) and D(2) still unknown}
94      B(2) = Bo(2)-dy;
95
96      % determine rotation of bar BC
97      rotBC = atan((Co(2)-Bo(2))/(Bo(1)-Co(1)))-atan((C(2)-B(2))/...
98          (B(1)-C(1)));
99      % determine new position of xBC,yBC
100     temp = rot_ccw([xBCo-Bo(1),yBCo-Bo(2)],rotBC);
101     xBC = B(1)+temp(1);
102
103     % determine thrust from equilibrium of BC
104     H = (vAC*(C(1)-B(1))-vBC*(xBC-B(1)))/(B(2)-C(2));
105
106     % determine rd -> D(1), D(2)
107     xCD = xCDo+dx;
108     rd = (vCD*(xCD-C(1))+H*C(2)+v_tot*(C(1)-dx))/...
109         (v_tot*sin(alpha)+H*cos(alpha));
110     D = [rd*sin(alpha)+dx, rd*cos(alpha)];
111
112     % check global equilibrium, by checking validity of rd
113     valid = range_check(0,ro*sin(alpha)+dx,D(1));
114
115     if valid == 1
116         H_increase(i) = H;
117         spread(i) = dx/(ri*sin(alpha));
118         dip(i) = dy/ri;
119         B_track(i,:) = B;
120         C_track(i,:) = C;
121         D_track(i,:) = D;
122         rotBC_track(i) = rotBC;
123         Co_track(i,:) = Co;
124         vAB_track(i) = vAB;
125         vAC_track(i) = vAC;
```

```
126         xBC_track(i) = xBC;
127     else
128         mode = 'D is invalid';
129     end
130     i = i+1;
131 end
132
133 a = mod(i-2,4);
134 % change 'final' designation to 50%
135 spread_final = spread((i-2-a)*position/4)*100;
136 dx_final = spread((i-2-a)*position/4)*(ri*sin(alpha));
137 dip_final = dip((i-2-a)*position/4)*100;
138 dy_final = dip((i-2-a)*position/4)*ri;
139 H_final = H_increase((i-2-a)*position/4);
140 H_Hmin = H_increase((i-2-a)*position/4)/H_min;
141
142 % pick out points at 50%
143 B_final = B_track((i-2-a)*position/4,:);
144 C_final = C_track((i-2-a)*position/4,:);
145 D_final = D_track((i-2-a)*position/4,:);
146 rotBC_final = rotBC_track((i-2-a)*position/4);
147 Co_final = Co_track((i-2-a)*position/4,:);
148 vAB_final = vAB_track((i-2-a)*position/4);
149 vAC_final = vAC_track((i-2-a)*position/4);
150 xBC_final = xBC_track((i-2-a)*position/4);
151
152 n=180;
153 %%%%%%%%%%%%%%%%%%%%%%%%%%%%%%%%%%%%%%%%%%%%%%%%%%%%%%%%%%%%%%%%%%%%%%%%%%%
154 intrados = intrados - 10*pi/180;
155 % new position for C (displaced) and rotation of BC
156 Co_final = [ri*sin(intrados), ri*cos(intrados)];
157 C_final =  Co_final+[dx_final, 0];
158 rotBC_final = atan((Co_final(2)-Bo(2))/...
159     (Bo(1)-Co_final(1)))-atan((C_final(2)-B_final(2))/...
160     (B_final(1)-C_final(1)));
161 % update vAC, vBC, xBC_final
162 [~,~,vAC] = segment_properties_EES(ri,ro,0,intrados);
163 [xBCo,yBCo,vBC] = segment_properties_EES(ri,ro,extrados,intrados);
164 temp = rot_ccw([xBCo-Bo(1),yBCo-Bo(2)],rotBC);
165 xBC_final = B(1)+temp(1);
166
167 load = 0;
168 h=0;
```

```
169 valid = 1;
170 while (valid == 1)
171
172     valid = 0;
173     load = load+1;
174     % apply load to one degree segment BE
175     % point of load application
176     temp = rot_ccw(([0,-dy_final]-B_final),rotBC_final);
177     O = B_final+temp;
178     pointE = extrados+pi/180;
179     [x_cg,y_cg,volE] = segment_properties_EES(ri,ro,extrados,pointE);
180     % calculate rotated cg of BE wrt shifted center of segment
181     temp = rot_ccw([x_cg,y_cg]-Bo,rotBC_final);
182     xBb = temp(1)+B_final(1)-O(1);
183
184     % determine thrust from equilibrium of BC
185     H_final = ((vAC+load)*(C_final(1)-B_final(1))-...
186         vBC*(xBC_final-B_final(1))-load*(temp(1)))/...
187         (B_final(2)-C_final(2));
188     h=h+1;
189     H_track(h)=H_final;
190
191     % initialize counter for thrust line tracking
192     j_max = round(n*(intrados-pointE)/2/alpha);
193     xy2=zeros(j_max,2);
194     r=zeros(j_max,1);
195
196     % find equilibrium for BE
197     j=1;
198     phi2 = pointE;
199     r(j) = (H_final*(B_final(2)-O(2))+(load+volE)*xBb+vAB_final*(B_final
          (1)-O(1)))/...
200         ((vAB_final+load+volE)*sin(phi2-rotBC_final)+H_final*cos(phi2-
              rotBC_final));
201     xy2(j,:) = [r(j)*sin(phi2-rotBC_final)+O(1),r(j)*cos(phi2-
          rotBC_final)+O(2)];
202     E_final = xy2(1,:);
203     E = phi2*180/pi;
204
205     % thrust in EC
206     for j = 2:j_max
207         phi2 = pointE+(intrados-pointE)/j_max*j;
208         [x_cg,y_cg,vol] = segment_properties_EES(ri,ro,pointE,phi2);
```

```
209
210         % calc rotated cg of segment EC
211         temp = rot_ccw([x_cg,y_cg]-E_final,rotBC_final);
212         xBb = temp(1)+E_final(1)-O(1);
213         % define x,y coordinates for thrust line
214         r(j) = (H_final*(E_final(2)-O(2))+vol*xBb+(vAB_final+load+volE)
              *(E_final(1)-O(1)))/...
215             ((vAB_final+vol+load+volE)*sin(phi2-rotBC_final)+H_final*cos
                (phi2-rotBC_final));
216         xy2(j,:) = [r(j)*sin(phi2-rotBC_final)+O(1),r(j)*cos(phi2-
              rotBC_final)+O(2)];
217     end
218
219
220     % thrust in CD
221     j_max = round(n*(alpha-intrados)/2/alpha);
222     xy3=zeros(j_max,2);
223     r=zeros(j_max,1);
224     for j = 1:j_max
225         phi2 = intrados+(alpha-intrados)/j_max*j;
226         [x_cg,~,vol] = segment_properties_EES(ri,ro,intrados,phi2);
227
228         r(j) = (vol*(x_cg-Co_final(1))+H_final*Co_final(2)+(vAC_final+
              vol+load)*...
229             Co_final(1))/(H_final*cos(phi2)+(vAC_final+vol+load)*sin(
                phi2));
230         xy3(j,:) = [r(j)*sin(phi2)+dx_final,r(j)*cos(phi2)];
231         D_final = xy3(j,:);
232     end
233
234     % stop when thrust line reaches extrados (at abutment)
235     if max(r)>=ro
236         valid = 0;
237     else
238         valid = 1;
239     end
240 end
241 %Load conversion from area to N, 19 is area of one deg slice with R=100,
242 %0.049 is weight of one deg slice of model block
243 load=load/19.186*0.049
244 %remove ; for tracking
245 Co_track;
246 r;
```

```
247 xy2;
248 E_final;
249 E;
250 H_track';
251 spread_for_leg = ['Spread to ',int2str(position*25),'% of collapse'];
252 %%%%%%%%%%%%%%%%%%%%%%%%%%%%%%%%%%%%%%%%%%%%%%%%%%%%%%%%%%%%%%%%%%%%%%%%%%%%
253
254 if figs == 1
255     %%%%%%%%%%%%%%%%%%%%%%%%%%%%%%%%%%%%%%%%%%%%%%%%%%%%%%%%%%%%%%%%%%%%%%%%%%%
256     % PLOT DEFORMED GEOMETRY
257     barrel = segment_outline(ri,ro,pi/2,pi/2-alpha,0,0,0);
258     % AB
259     AB = segment_outline(ri,ro,pi/2,pi/2-extrados,0,-dy_final,0);
260     % CD
261     CD = segment_outline(ri,ro,pi/2-intrados,pi/2-alpha,dx_final,0,0);
262     % BC
263     BC = segment_outline(ri,ro,pi/2-extrados,pi/2-intrados,0,0,0);
264     temp = rot_ccw([BC(:,1)-Bo(1),BC(:,2)-Bo(2)],rotBC_final);
265     BC = [temp(:,1)+Bo(1),temp(:,2)+B_final(2)];
266
267     %plot
268     figure(2)
269     plot(barrel(:,1),barrel(:,2),'k:','LineWidth',1);
270     hold on;
271     plot(AB(:,1),AB(:,2),'g',BC(:,1),BC(:,2),'g',CD(:,1),CD(:,2),'g',...
272         'LineWidth',2);
273     hold on;
274     plot([B_final(1);xy2(:,1)],[B_final(2);xy2(:,2)],'r',...
275         [C_final(1);xy3(:,1)],[C_final(2);xy3(:,2)],'r');
276     hold on;
277     plot(D_final(1),D_final(2),'k.',C_final(1),C_final(2),'k.',...
278         B_final(1),B_final(2),'k.','MarkerSize',20);
279
280     axis equal;
281     axis([0 1.1*ro 0 1.1*ro]);
282
283     legend('Undeformed State',num2str(spread_for_leg),'location','
        northeast')
284     title(fig2_title);
285
286     text(.97*ri,2,['Span increase = ',num2str(spread((i-2-a)*position/4)
        *100),'%'],...
```

```
287          'VerticalAlignment','bottom','HorizontalAlignment','center','
               FontSize',10)
288      text(.97*C_final(1),.97*C_final(2),[int2str(intrados*180/pi),'\circ'
         ],...
289          'VerticalAlignment','top','HorizontalAlignment','right','
               FontSize',10)
290      text(1.03*B_final(1),1.03*B_final(2),[int2str(extrados*180/pi),'\
         circ'],...
291          'VerticalAlignment','bottom','HorizontalAlignment','left','
               FontSize',10)
292      text(2,2,['Load capacity = ',num2str(load),' N'],...
293          'VerticalAlignment','bottom','HorizontalAlignment','left','
               FontSize',10)
294
295  end
296
297  end
```

C.3 Barrel Minimum Thrust

```
%%%%%%%%%%%%%%%%%%%%%%%%%%%%%%%%%%%%%%%%%%%%%%%%%%%%%%%%%%%%%%%%%%%%%%%%%%%%
% Adapted from function written by Jennifer Zessin and presented in: %
% Zessin, J. (2012). Collapse analysis of unreinforced masonry       %
% domes and curving walls . Ph.D. thesis, MIT.                        %
%%%%%%%%%%%%%%%%%%%%%%%%%%%%%%%%%%%%%%%%%%%%%%%%%%%%%%%%%%%%%%%%%%%%%%%%%%%%

function [H_min,v_tot,hinges]  = barrel_min_thrust (alpha,t_R,n,figs)

close all;

fig_title = ['Limiting Thrust State for \alpha = ',int2str(alpha),...
    '\circ, t/R = ',num2str(t_R)];

%%%%%%%%%%%%%%%%%%%%%%%%%%%%%%%%%%%%%%%%%%%%%%%%%%%%%%%%%%%%%%%%%%%%%%%%%%%%
% DEFINE GEOMETRY PARAMETERS
% embrace
alpha = alpha*pi/180;
% t and R properties
R = 100;
t = R*t_R;
ri = R-t/2;
ro = R+t/2;
%%%%%%%%%%%%%%%%%%%%%%%%%%%%%%%%%%%%%%%%%%%%%%%%%%%%%%%%%%%%%%%%%%%%%%%%%%%%
% DETERMINE MIN THRUST STATE - NO SPREAD
% initialize min thrust
H_min = 10^10;

% discretization
m_max = 50;
k_max = m_max;

d_phi = 2*alpha/n;

[x_cg_tot,~,v_tot] = segment_properties_EES(ri,ro,0,alpha);

% search for a valid min thrust state
for k = 1:k_max+1
for m = 1:m_max+1

    % define thrust line position at crown and springing
```

```
41      rise = ro-t*(k-1)/k_max;
42      run = ro-t*(m-1)/m_max;
43
44      % calc H for given thrust line constraints
45      H = v_tot*(run*sin(alpha)-x_cg_tot)/(rise-run*cos(alpha));
46
47      % define x,y coordinates for thrust line
48      max_count = ceil(n/2)+1;
49      xy=zeros(max_count,2);
50      r=zeros(max_count,1);
51
52      xy(1,:) = [0,rise];
53      r(1,:) = rise;
54
55      if mod(n,2)
56          phi2_2 = d_phi/2;
57      else
58          phi2_2 = d_phi;
59      end
60      [x_cg,~,vol]=segment_properties_EES(ri,ro,0,phi2_2);
61
62      r(2,:) = (H*rise+vol*x_cg)/(vol*sin(phi2_2)+H*cos(phi2_2));
63      xy(2,:) = r(2)*[sin(phi2_2),cos(phi2_2)];
64
65      for j = 3:max_count
66          phi2 = phi2_2 + d_phi*(j-2);
67          [x_cg,~,vol]=segment_properties_EES(ri,ro,0,phi2);
68
69          r(j,:) = (H*rise+vol*x_cg)/(vol*sin(phi2)+H*cos(phi2));
70          xy(j,:) = r(j)*[sin(phi2),cos(phi2)];
71      end
72
73      % check validity of thrust state and check if min/max, store info
74      valid_min = range_check(ri,ro,r);
75      if (valid_min == 1) && (H < H_min)
76          H_min = H;
77          xy_final_min = xy;
78          r_final_min = r;
79      end
80  end
81  end
82
83  %%%%%%%%%%%%%%%%%%%%%%%%%%%%%%%%%%%%%%%%%%%%%%%%%%%%%%%%%%%%%%%%%%%%%%%%%%%%%%%
```

```
84 within = 5;
85 percent = (r_final_min-ri)./t*100;
86 index_test1 = percent > 100-within;
87 index_test2 = percent < within;
88 %%%%%%%%%%%%%%%%%%%%%%%%%%%%%%%%%%%%%%%%%%%%%%%%%%%%%%%%%%%%%%%%%%%%%%%%%%%%
89 % determine intrados and extrados hinges
90 [~,min_index] = min(r_final_min);
91 [~,max_index] = max(r_final_min(1:max_count-1));
92
93 max_index2 = find(index_test1,1,'last');
94 min_index2 = find(index_test2(max_index2:max_count),1,'first');
95 min_index2 = max_index2+min_index2-1;
96
97 if mod(n,2)
98 %     hinges = d_phi*180/pi*[(max_index-1.5),(min_index-1.5)];
99     hinges = d_phi*180/pi*[(max_index2-1.5),(min_index2-1.5)];
100 else
101 %     hinges = d_phi*180/pi*[(max_index-1),(min_index-1)];
102     hinges = d_phi*180/pi*[(max_index2-1),(min_index2-1)];
103 end
104 %%%%%%%%%%%%%%%%%%%%%%%%%%%%%%%%%%%%%%%%%%%%%%%%%%%%%%%%%%%%%%%%%%%%%%%%%%%%
105
106 if figs ==1
107
108     barrel = segment_outline(ri,ro,pi/2,pi/2-alpha,0,0,0);
109
110     %plot
111     figure(1);
112     plot(barrel(:,1),barrel(:,2),'b','LineWidth',2.5);
113     hold on;
114     plot(xy_final_min(:,1),xy_final_min(:,2),'r.:');
115     hold on;
116
117     % hold on;
118     axis(1.1*ro*[0 1 0 1]);
119     axis square;
120
121     legend('Barrel','Minimum Thrust')%,'Hinge Location');
122     title(fig_title);
123 end
124 end
```

C.4 Arch Segment Outline

```
% creates vector of dome outline {all angle inputs are in radians}

%%%%%%%%%%%%%%%%%%%%%%%%%%%%%%%%%%%%%%%%%%%%%%%%%%%%%%%%%%%%%%%%%%%%%%%%%%%%
% Used with permission from Jennifer Zessin                                   %
% Zessin, J. (2012). Collapse analysis of unreinforced masonry               %
% domes and curving walls . Ph.D. thesis, MIT.                                %
%%%%%%%%%%%%%%%%%%%%%%%%%%%%%%%%%%%%%%%%%%%%%%%%%%%%%%%%%%%%%%%%%%%%%%%%%%%%

function [segment_outline_vector] = segment_outline(ri,ro,start_angle
  ,end_angle,x_shift,y_shift,ccw_rotation)

% corner_points = [x_ro_start,y_ro_start;x_ro_end,y_ro_end;x_ri_end,
  y_ri_end;x_ri_start,y_ri_start]
corner_points = [ro*cos(start_angle);
                 ro*cos(end_angle);
                 ri*cos(end_angle);
                 ri*cos(start_angle)];

x_ro = (corner_points(1):(corner_points(2)-corner_points(1))/1000:
  corner_points(2))';
y_ro = sqrt(ro^2-x_ro.^2);

x_ri = fliplr(corner_points(4):(corner_points(3)-corner_points(4))/1000:
  corner_points(3))';
y_ri = sqrt(ri^2-x_ri.^2);

segment_outline_vector = [cat(1,x_ro,x_ri,x_ro(1))+x_shift,cat(1,y_ro,
  y_ri,y_ro(1))+y_shift];

if ccw_rotation == 0
else
    segment_outline_vector = rot_ccw(segment_outline_vector,ccw_rotation
      );
end

end
```

C.5 Arch Segment Properties

```
% Calculate the centroid position of a segment of an arch,
% bounded by ri,ro and phi1,phi2

function [x_cg,y_cg,area] = segment_properties_EES(ri,ro,phi1,phi2)


phi = phi2 - phi1;
area = (ro^2 - ri^2)*phi/2;

r_cg = 4*sin(phi/2)*(ro^3-ri^3)/(3*phi*(ro^2-ri^2));
x_cg = r_cg*sin(phi1+phi/2);
y_cg = r_cg*cos(phi1+phi/2);

end
```

C.6 Counter-clockwise Vector Rotation

```
% rotates a vector [x1,y1;x2,y2;...]
% ccw by a specified amount 'a' in radians

%%%%%%%%%%%%%%%%%%%%%%%%%%%%%%%%%%%%%%%%%%%%%%%%%%%%%%%%%%%%%%%%%%%%%%%%%%%
% Used with permission from Jennifer Zessin                               %
% Zessin, J. (2012). Collapse analysis of unreinforced masonry            %
% domes and curving walls . Ph.D. thesis, MIT.                            %
%%%%%%%%%%%%%%%%%%%%%%%%%%%%%%%%%%%%%%%%%%%%%%%%%%%%%%%%%%%%%%%%%%%%%%%%%%%

function [rotated_vector] = rot_ccw(vector,angle)

rotated_vector = ([cos(angle),-sin(angle);sin(angle),cos(angle)]...
    *vector')';

end
```